

# Trileucine as a Dispersibility Enhancer of Spray-Dried Inhalable Microparticles

Mani Ordoubadi<sup>1</sup>, Florence K. A. Gregson<sup>2</sup>, Hui Wang<sup>1</sup>, Nicholas B. Carrigy<sup>3</sup>, Mark Nicholas<sup>4</sup>, Sandra Gracin<sup>4</sup>, David Lechuga-Ballesteros<sup>3</sup>, Jonathan P. Reid<sup>2</sup>, Warren H. Finlay<sup>1</sup>, Reinhard Vehring<sup>1,\*</sup>

<sup>1</sup>Department of Mechanical Engineering, University of Alberta, Edmonton, Alberta, Canada

<sup>2</sup>School of Chemistry, University of Bristol, Bristol, United Kingdom

<sup>3</sup>Inhalation Product Development, Pharmaceutical Technology & Development, Operations, AstraZeneca, South San Francisco, California, USA

<sup>4</sup>Inhalation Product Development, Pharmaceutical Technology & Development, Operations, AstraZeneca, Gothenburg, Sweden

Corresponding author:

Reinhard Vehring

University of Alberta, Department of Mechanical Engineering, 10-203 Donadeo Innovation Centre for Engineering, 9211 116th Street NW, Edmonton, Alberta T6G 1H9, Canada

[reinhard.vehring@ualberta.ca](mailto:reinhard.vehring@ualberta.ca)

## 18 **Abstract**

19 The formation of trileucine-containing spray-dried microparticles intended for pulmonary delivery was  
20 studied in depth. A single-particle method was employed to study the shell formation characteristics of  
21 trileucine in the presence of trehalose as a glass former, and an empirical correlation was proposed to  
22 predict the instance of shell formation. A droplet chain instrument was used to produce and collect  
23 monodisperse particles to examine morphology and calculate particle density for different levels of  
24 trileucine. It was observed that the addition of only 0.5 mg/mL (10% w/w) trileucine to a trehalose system  
25 could lower dried particle densities by approximately 1 g/cm<sup>3</sup>. In addition, a laboratory-scale spray dryer  
26 was used to produce batches of trileucine/trehalose powders in the respirable range. Raman spectroscopy  
27 demonstrated that both components were completely amorphous. Scanning electron microscopy and time-  
28 of-flight secondary ion mass spectrometry were used to study the particle morphologies and surface  
29 compositions. For all cases with trileucine, highly rugose particles with trileucine coverages of more than  
30 60% by mass were observed with trileucine feed fractions of as little as 2% w/w. Moreover, it was seen  
31 that at lower trileucine content, smaller and larger particles of a polydisperse powder had slightly different  
32 surface compositions. The surface activity of trileucine was also modeled via a modified form of the  
33 diffusion equation inside an evaporating droplet that took into account initial surface adsorption and  
34 eventual surface desorption due to droplet shrinkage. Finally, using the Flory-Huggins theory, it was  
35 estimated that at room temperature, liquid-liquid phase separation would start when the trileucine reached  
36 an aqueous concentration of about 18 mg/mL. Besides the surface activity of trileucine, this low  
37 concentration was assumed to explain the substantial effect of trileucine on the morphology of spray-dried  
38 particles due to early phase separation. The methodology proposed in this study can be used in the  
39 rational design of trileucine-containing microparticles.

40

41 **Keywords:** Spray drying, Trileucine, Surface activity, Particle engineering, Particle formation.

42

## 43 **1. Introduction**

44 Spray drying is a continuous process of producing fine powder with a controlled size distribution through  
45 the rapid evaporation of a feed solution, suspension, or emulsion after atomization into a hot drying gas  
46 [1]. This production method is particularly useful in the preparation of microparticles containing  
47 pharmaceutical actives or biologics because of its accurate control of the outlet conditions, particle  
48 morphology, and size distributions [2]. Effective pulmonary delivery of dry powder necessitates specific  
49 particle characteristics for maximum delivery efficiency and therapeutic efficacy: 1) an approximate  
50 range of 1 to 5 micrometers in aerodynamic diameter for delivery to the lungs [3,4], 2) acceptable  
51 physical and chemical stability for long-term shelf storage, and 3) low interparticle cohesion to allow for  
52 good dispersion and deagglomeration with minimal loss in the delivery device and the upper respiratory  
53 tract [5]. To achieve these properties, appropriate formulation excipients are used. For example, glass  
54 formers such as trehalose have been used both as bulking agents and as stabilizers of the biological  
55 components [6–8]. To improve the aerosolization characteristics of the powder, a specific class of  
56 excipients labeled as shell formers or dispersibility enhancers have been used; these include leucine [7,9–  
57 11] and trileucine [12–14].

58 Trileucine is a tripeptide composed of three leucine residues and is used in the spray drying of  
59 pharmaceutical microparticles mostly as a dispersibility enhancer to produce low-density, non-cohesive  
60 and rugose particles [13,15,16]. It is a strongly surface-active material, typically does not crystallize  
61 during spray drying nor upon storage, and has a low aqueous solubility of about 6.8 mg/mL at neutral pH  
62 [12]. These characteristics have been reported to be responsible for considerable increase of surface  
63 roughness and efficient dispersibility enhancement of particles containing small quantities of trileucine in  
64 the formulation [13,14,17]. Furthermore, the high surface coverage of trileucine in spray-dried particles  
65 and its high glass transition temperature of ~104 °C are believed to responsible for its considerable

66 improvement in the stability of biologics and bacteriophages during production and upon storage [12,17].  
67 Due to the high surface activity of trileucine, the molecules adsorbed on the droplet surface are believed  
68 to have their hydrophobic tails directed outwards, a feature that may explain the observed moisture  
69 protection features of trileucine [14].

70 Given its aforementioned properties, trileucine can be considered a dispersibility-enhancing excipient  
71 with far-reaching benefits. The disadvantage of using trileucine is its current high price compared to that  
72 of other less effective alternatives such as leucine. Hence, it is desirable to include as little trileucine as  
73 possible in the formulation while still meeting the design criteria. Also, the use of particle formation  
74 models becomes relevant here, as they allow reductions in the number of experimental iterations during  
75 the formulation development by predicting the sequence of surface accumulation and solidification of  
76 different excipient and actives [15,18]. The use of such models is less complicated for excipients and  
77 actives that are not surface-active and do not crystallize during spray drying [15], e.g. trehalose [19],  
78 pullulan [8], and budesonide [20]. These models have been extended to crystallizing components [21], but  
79 the incorporation of surface activity into such models has not been achieved. Further, observations that a  
80 non-surface-active dipeptide (L-tyrosyl-L-isoleucine) with low solubility, very close to the solubility of  
81 trileucine, can dry into low-density amorphous particles suggest that surface activity alone cannot be  
82 responsible for the shell formation properties of trileucine and that amorphous phase separation must also  
83 contribute [19,22]. The formation of particles containing trileucine is complex and cannot be described  
84 comprehensively by the current particle formation models. More information is required for the prediction  
85 of the instances of shell formation and surface coverage of trileucine in a successful rational design of the  
86 formulation.

87 To address the aforementioned complexities, three different and complementary experimental methods  
88 are employed here to study the particle formation characteristics of trileucine in the presence of trehalose  
89 as a glass former. These tools were previously used together successfully in explaining the particle  
90 formation of leucine [11]. A Comparative-Kinetics Electrodynamic Balance (CK-EDB) was used to

91 measure the approximate time of shell formation from instantaneous sizing of single aerosol droplets  
92 trapped in a controlled environment [23,24]. A monodisperse droplet chain instrument was also used to  
93 collect the dried particles for electron microscopy and measurement of the particle densities [24–26].  
94 Furthermore, a lab-scale spray dryer was used to produce powders with diameters in the respirable range  
95 and to produce enough material for further characterization techniques. The effect of surface activity of  
96 trileucine and its mechanism of phase separation are also predicted theoretically.

97

## 98 **2. Materials and Methods**

### 99 **2.1. Materials**

100 The spray-dried solutions were prepared using HPLC grade water (Cat. No. W5-4, Fisher Scientific,  
101 Ottawa, ON, Canada) with total solids contents ranging from 1 to 50 mg/mL and the appropriate fractions  
102 of trehalose and trileucine. Crystalline D-(+)-trehalose dihydrate was bought directly from the vendor  
103 (Cat. No. BP2687-1, Fisher Scientific, Ottawa, ON, Canada), while spray-dried amorphous trileucine was  
104 used in solution preparation to avoid issues with low solubility. Raw crystalline trileucine (Cat. No. H-  
105 3915, Bachem, Torrance, CA, USA) was used in the preparation of the amorphous batch.

106

### 107 **2.2. Experimental Methods**

#### 108 **2.2.1. Comparative-Kinetics Electrodynamic Balance (CK-EDB)**

109 A comparative-kinetics electrodynamic balance was used to estimate the shell formation behavior of  
110 trileucine-containing systems. The evaporation and solidification behavior of single solution droplets  
111 ( $d_0 \sim 50 \mu\text{m}$ ) were analyzed in a comparative-kinetics electrodynamic balance [11,23,24]. For each  
112 experiment, a droplet-on-demand dispenser (MJ-ABP-01, MicroFab Technologies, Plano, Texas, USA)  
113 generated a single droplet, charged on generation by applying a DC voltage to an electrode near the tip.

114 The droplet was then trapped inside a controlled environment with the help of an AC potential difference  
 115 applied via two sets of concentric cylindrical electrodes mounted vertically opposite one another. The  
 116 drag force from a gas flow and the gravitational force on the droplet were counteracted by applying an  
 117 additional DC voltage to the bottom electrodes that was dynamically controlled to account for the change  
 118 in droplet mass during drying. A 532 nm green continuous-wave diode laser (Ventus, Laser Quantum,  
 119 Stockport, UK) illuminated the particle, producing a scattered pattern and a phase-function both of which  
 120 were captured on a CCD every ~10 ms at a forward scattering angle of 45° over a range of 24°. The  
 121 instantaneous size of the droplet was measured within an accuracy of ±100 nm using the fringe spacing in  
 122 the obtained phase-functions and the geometric-optics approximation to Mie theory [23]. The morphology  
 123 of the particle during drying was also approximated by analyzing the irregularities in the phase-function  
 124 [27]. The instance of solidification and shell formation was then determined from the instantaneous  
 125 morphology data and deviation from a constant evaporation rate [11].

126 The studied formulations using the EDB instrument are presented in Table 1. For each case, three to four  
 127 droplets were studied at a chamber temperature of 20 °C and relative humidity of ~35%. The formulations  
 128 were selected so that the occurrence of solidification and shell formation would be at sufficiently large  
 129 diameters for detection in the CK-EDB instrument and the trileucine concentrations would cover low to  
 130 high initial saturations. The low drying temperature and high humidity level were chosen based on the  
 131 instrument limitations and to result in high temporal resolution during the measurements.

132 *Table 1* The samples studied using the electrodynamic balance, accompanied by their compositions, trileucine initial saturation  
 133 (based on a solubility of 6.8 mg/mL), and measured average initial droplet diameters. The drying temperature was set to 20 °C  
 134 and the relative humidity was ~35% for all cases. The uncertainties of the initial droplet diameters are the standard deviation of  
 135 multiple droplets studied for each case.

Sample Name	Total Solids Content (mg/mL)	Trehalose Mass Fraction (%)	Trileucine Mass Fraction (%)	Trileucine Initial Saturation (-)	$d_0$ (µm)
-------------	------------------------------------	-----------------------------------	---------------------------------	---	------------

EDB1TL100	1	0	100	0.15	53.8±0.0
EDB2TL100	2	0	100	0.29	52.9±0.1
EDB5TL100	5	0	100	0.73	53.0±0.2
EDB5T100	5	100	0	0.00	53.6±0.2
EDB5T90TL10	5	90	10	0.07	52.6±0.0
EDB5T80TL20	5	80	20	0.15	52.6±0.3
EDB5T70TL30	5	70	30	0.22	53.3±0.1
EDB5T50TL50	5	50	50	0.37	53.7±0.0

136

### 137 2.2.2. Monodisperse Droplet Chain Instrument

138 A droplet chain instrument was used to produce and collect monodisperse microparticles [8,24,25,28]. A  
139 droplet-on-demand piezoelectric dispenser with an orifice diameter of 40 µm (MJ-AL-HT-40-8MX,  
140 MicroFab Technologies, Plano, Texas, USA) injected droplets into a glass tube with a frequency of 60  
141 Hz. Dry air passed through the flow tube from above with a flow rate of 10 to 15 L/min and a temperature  
142 of approximately 20 °C. Dried particles falling down the tube were then collected on a membrane filter  
143 with a pore size of 0.8 µm (Isopore Polycarbonate, Millipore, Darmstadt, Germany) attached on an SEM  
144 stub with a hole drilled in the center and connected to a vacuum source. An imaging system was used to  
145 measure the initial droplet diameters. Approximately two hundred images were taken at the start and near  
146 the end of each experiment; these were then analyzed using MATLAB [29] to calculate the average initial  
147 droplet diameter and the corresponding standard deviation of each case. The formulations studied using  
148 the monodisperse droplet chain instrument were chosen in such a way as to produce particles  
149 approximately resembling the final dried particles of the CK-EDB measurements and are presented in  
150 Table 2.

151 *Table 2* The samples studied using the droplet chain instrument, accompanied by their compositions, trileucine initial saturation  
 152 (based on a solubility of 6.8 mg/mL), and measured average initial droplet diameters. The drying temperature was approximately  
 153 20 °C for all cases. The uncertainties of the initial droplet diameters are the standard deviations of two hundred droplets per case.

Sample Name	Total Solids Content (mg/mL)	Trehalose Mass Fraction (%)	Trileucine Mass Fraction (%)	Trileucine Initial Saturation (-)	$d_0$ ( $\mu\text{m}$ )
MDC1TL100	1	0	100	0.15	36.2 $\pm$ 0.3
MDC2TL100	2	0	100	0.29	34.5 $\pm$ 0.6
MDC5TL100	5	0	100	0.73	38.8 $\pm$ 0.2
MDC10T100	10	100	0	0	42.4 $\pm$ 0.1
MDC5T90TL10	5	90	10	0.07	34.9 $\pm$ 0.3
MDC5T80TL20	5	80	20	0.15	36.8 $\pm$ 0.2
MDC5T50TL50	5	50	50	0.37	35.9 $\pm$ 0.2

154

155 **2.2.3. Spray Drying**

156 The spray-dried powders were manufactured using a modified laboratory-scale spray dryer (B-191, Büchi  
 157 Labortechnik AG, Flawil, Switzerland) with a customized twin-fluid atomizer [8]. For all formulations,  
 158 the inlet temperature was set to 75 °C, the atomizer had an air-to-liquid ratio of 10, the drying gas flow  
 159 rate was set to 540 L/min, and the liquid feed flow rate was 2.5 mL/min. These process parameters  
 160 resulted in an outlet temperature of about 49 °C and a predicted outlet relative humidity of about 7% [11].  
 161 For the specific twin-fluid atomizer used, the initial mass median diameter of the atomized droplets was  
 162 estimated to be around 8  $\mu\text{m}$  [30]. The powders collected in the cyclone were then stored in dry  
 163 conditions (RH ~ 0%) at room temperature. The compositions of the spray-dried formulation are shown in  
 164 Table 3. These compositions were chosen to cover a range from low to high trileucine initial saturations  
 165 and to produce particles in the respirable range.

166 *Table 3* The compositions of the spray-dried formulations. Inlet temperature was 75 °C for all cases and the estimated mass  
167 median diameter of the atomized droplets was ~8 μm.

Sample	Total Solids Content (mg/mL)	Trehalose Mass Fraction (%)	Trileucine Mass Fraction (%)	Trileucine Initial Saturation (-)
SD50T100	50	100	0	0
SD50T98TL2	50	98	2	0.15
SD50T95TL5	50	95	5	0.37
SD50T90TL10	50	90	10	0.73

168

## 169 2.3. Characterization Techniques

### 170 2.3.1. Scanning Electron Microscopy

171 A field emission scanning electron microscope (Sigma FESEM, Zeiss, Jena, Germany) was used to obtain  
172 the micrographs for this study. The accelerating voltage was 5 kV, and working distances ranged from 6.5  
173 to 8.5 mm. The samples were placed on aluminum SEM stubs and coated with a vacuum gold sputter  
174 (Desk II, Denton Vacuum LLC, Moorestown, NJ, USA).

175 The monodisperse particles collected from the droplet chain instrument were sized from the SEM  
176 micrographs via manual calculation of the projected area of about 40 particles per sample using ImageJ  
177 software [31]. The resulting projected area diameter is theoretically equal to the volume equivalent-  
178 diameter only if the particles are spherical. In the case of highly folded particles, this method provides an  
179 approximate diameter.

180

### 181 2.3.2. Raman Spectroscopy

182 The solid phases of the spray-dried powders were determined using a custom-built dispersive Raman  
183 spectrometer, the operation and design of which have been explained elsewhere [32]. Raw crystalline

184 materials were analyzed to provide the reference spectra for crystalline trehalose and trileucine, and  
185 spray-dried trehalose and trileucine powders were used as their amorphous reference spectra [13].

186

### 187 2.3.3. Time-of-Flight Secondary Ion Mass Spectrometry

188 A TOF-SIMS instrument (TOF.SIMS<sup>5</sup>, ION-TOF GmbH, Münster, Germany) with a Bi<sub>3</sub><sup>+</sup> source  
189 operating at 30 keV energy was used to measure the surface compositions of the spray-dried particles to  
190 an average depth of 3-5 nm [33]. Each measurement was performed on a raster of 200 μm × 200 μm with  
191 a frame of 1024×1024 pixels. The data processing was performed on bins of 512×512 pixels of the  
192 original frames. The raw materials were also analyzed to give the reference spectrum of each component.  
193 The pixel compositions were then obtained by fitting the spectrum to a linear combination of the  
194 reference spectra. More details on the post-processing of the TOF-SIMS data can be found elsewhere  
195 [34].

196 The processed data were then converted to 8-bit RGB images with the pixel strength of each component  
197 giving the respective color intensity (0-255). The resulting images were analyzed to find the average  
198 surface compositions of the whole powder, as well as small ( $d_p < 1 \mu\text{m}$ ), medium ( $1 < d_p < 3 \mu\text{m}$ ), and  
199 large ( $d_p > 3 \mu\text{m}$ ) particle fractions. More details about the methodology with which the particles were  
200 sized and binned are given elsewhere [11].

201

## 202 2.4. Theoretical Aspects of Particle Formation

### 203 2.4.1. Particle Formation Theory for a Surface-Active Component

204 Trileucine is a surface-active material with a strong tendency to adsorb on the air-water interface and  
205 form a molecular monolayer. The approach used to predict the rate of surface adsorption of a surface-  
206 active material on the interface of an evaporating microdroplet is described below.

## 207 **The Equilibrium Surface Excess of Trileucine**

208 The surface adsorption of a surface-active material can be obtained from the equilibrium surface tension  
209 data at a specific temperature via the simplified Gibbs adsorption equation as follows [35]

$$\Gamma_{\text{eq}} = -\frac{1}{nRT} \cdot \frac{d\sigma}{d(\ln C)}, \quad (1)$$

210 where  $\Gamma_{\text{eq}}$  is the equilibrium surface excess in mol/m<sup>2</sup>,  $n = 1$  for non-ionic or zwitterionic solutes and  
211  $n = 2$  for one-by-one ionic solutes in the absence of any extra electrolyte [36],  $R$  is the universal gas  
212 constant,  $T$  is the solution temperature in K,  $\sigma$  is the surface tension in N/m, and  $C$  is the solute bulk  
213 concentration in mg/mL. For trileucine at pH levels close to the neutral value, the majority of the solute  
214 will be in zwitterionic form [12]; hence  $n$  is here assumed to be equal to 1.

215 The experimental tensiometry data are fitted using different empirical isotherms such as the Szyszkowski  
216 surface equation of state, defined as [36]

$$\sigma = \sigma_0 - nRT\Gamma_{\text{max}} \ln(1 + K_L C), \quad (2)$$

217 where  $\sigma_0$  is the surface tension of the neat solvent ( $\sim 72$  mN/m at 25 °C for water) and  $K_L$  is the Langmuir  
218 equilibrium adsorption constant. The combination of equations (1) and (2) results in the Langmuir  
219 isotherm, which gives the equilibrium surface excess values at different bulk concentrations as follows:

$$\Gamma_{\text{eq}} = \Gamma_{\text{max}} \left( \frac{K_L C}{1 + K_L C} \right). \quad (3)$$

220 The degree of surface activity of trileucine can be identified from the equilibrium surface tension data in  
221 Figure 1 [12]. The concentration dependence of the surface tension of aqueous trileucine solutions is  
222 shown for two temperatures of 25 °C and 45 °C, which represent typical droplet wet-bulb temperatures  
223 encountered in spray drying. Non-linear fits to equation (2) are shown in Figure 1 with  $\Gamma_{\text{max}} =$   
224  $2.8 \times 10^{-6}$  mol/m<sup>2</sup> (or 0.99 mg/m<sup>2</sup>) and  $K_L = 13.3$  mL/mg at 25 °C; and  $\Gamma_{\text{max}} = 2.4 \times 10^{-6}$  mol/m<sup>2</sup> (or  
225 0.87 mg/m<sup>2</sup>) and  $K_L = 15.5$  mL/mg at 45 °C. The amount of trileucine that can be adsorbed onto the air-  
226 water interface at different bulk concentrations can be estimated using equation 3. For a trileucine initial

227 bulk concentration of 0.5 mg/mL, the minimum value encountered in this study, the equilibrium surface  
228 excess is estimated to be around 0.9 of the maximum surface excess,  $\Gamma_{\max}$ . Hence, a maximum surface  
229 excess of 0.99 mg/m<sup>2</sup> at 25 °C will be used as a simplification in the subsequent calculations.

### 230 **Adsorption Kinetics of a Surface-Active Compound on an Evaporating Droplet**

231 The adsorption of the surface-active molecules is composed of three stages: diffusion of the molecules  
232 towards a domain immediately below the interface; adsorption of these molecules from this subsurface  
233 domain onto the interface; and, finally, reconfiguration of the molecules on the interface according to  
234 their hydrophobic/hydrophilic orientation [37,38]. For trileucine, a simple tripeptide, it can be assumed  
235 that surface adsorption kinetics are solely controlled by the diffusion of the molecules from the bulk to the  
236 surface. This is a reasonable assumption as the incorporation of such a small molecule into the adsorbed  
237 monolayer and the consequent reorientation is rapid [37]. In such a case, the minimum theoretical time to  
238 reach a specific surface excess,  $t_{\Gamma}$ , can be approximated from the Ward and Tordai equation [39,40]:

$$t_{\Gamma} = \frac{\pi\Gamma^2}{4C_b^2D}. \quad (4)$$

239 Here,  $D$  is the diffusion coefficient of the surface-active solute in the solution. Note that this equation was  
240 derived for a semi-infinite solution volume with a constant bulk concentration of  $C_b$ . This is not the case  
241 in a droplet during spray drying because the bulk concentration increases as the droplet shrinks. If the  
242 initial concentration of trileucine is used in conjunction with the maximum surface excess calculated  
243 previously, the time to reach surface saturation can be obtained as an approximate threshold. The values  
244 obtained from equation 4 are expected to be reasonable for large droplets but underestimate the actual  
245 timescale obtained from the solution of the diffusion equations inside a microdroplet. This may be  
246 explained by the fact that the amount of material needed to cover the surface relative to the available  
247 material inside the droplet increases as the initial droplet diameter decreases. Hence, for small atomized  
248 droplets, surface adsorption can deplete the surface-active material and cause the bulk concentration to  
249 decrease considerably, making the use of equation 4 questionable [41].

250 An accurate prediction of adsorption of a surface-active component during spray drying requires the  
 251 solution of the internal diffusion equation with appropriate boundary conditions. The adsorption of the  
 252 surfactant molecules from the subsurface domain to the interface causes a drop in the solute concentration  
 253 near the surface. This drop in local concentration induces a diffusional flux from the inside of the  
 254 evaporating droplet towards the surface as opposed to the diffusion from the surface to the center of the  
 255 droplet for non-surface-active solutes due to the evaporation and surface enrichment [18]. The adsorption  
 256 continues until the surface excess concentration reaches the maximum value,  $\Gamma_{\max}$ . Upon reaching this  
 257 maximum surface concentration, further shrinkage of the droplet surface due to evaporation causes  
 258 desorption of the molecules from the interface into the solution in order to maintain equilibrium, i.e.  $\Gamma =$   
 259  $\Gamma_{\max}$  [36].

260 The radial distribution due to the diffusion of a component,  $i$ , inside of an evaporating droplet can be  
 261 obtained via the solution of the following equation for conservation of mass [24]

$$\frac{\partial C_i}{\partial t} = \frac{4D_i}{d^2} \left( \frac{\partial^2 C_i}{\partial R^2} + \frac{2}{R} \frac{\partial C_i}{\partial R} \right) - \frac{\kappa R}{2d^2} \frac{\partial C_i}{\partial R}, \quad (5)$$

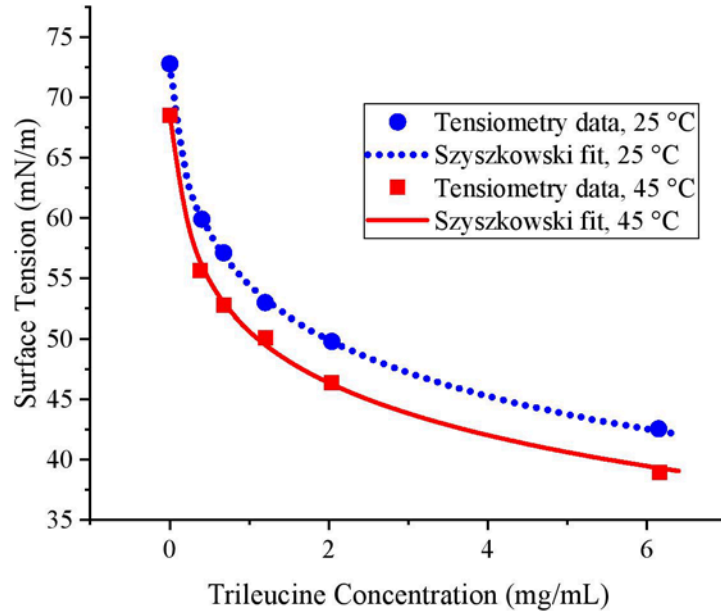
262 where  $C_i$  is the instantaneous concentration of this component at different radial coordinates,  $d$  is the  
 263 instantaneous droplet diameter,  $R = 2r/d$  is the dimensionless radial coordinate, and  $\kappa = -dd^2/dt$  is  
 264 the evaporation rate. The values of the evaporation rate for different drying temperatures can be found in  
 265 previous studies [11]. Equation 5 can be solved with the appropriate boundary conditions,  $\partial C_i/\partial R = 1$  at  
 266  $R = 0$  (droplet center) and  $\partial C_i/\partial R - Pe_i C_i = 0$  at  $R = 1$  (surface) for non-surface-active components  
 267 [19,24]. Here,  $Pe_i = \kappa/8D_i$  is the Péclet number of the  $i$ th component. The discretized physical domain  
 268 of a droplet, including the subsurface control volume and the adsorbed monolayer on the surface, is  
 269 shown schematically in Figure 2. For a surface-active material, the surface boundary condition needs to  
 270 be modified to account for the adsorption of the molecules onto the interface before reaching surface  
 271 saturation ( $\Gamma < \Gamma_{\max}$ ) as well as for desorption after reaching saturation ( $\Gamma = \Gamma_{\max}$ ). Here, some  
 272 assumptions are made to simplify the problem. First, before surface saturation, any material that reaches

273 the subsurface (the control volume at  $R = 1$ ) is instantaneously adsorbed onto the interface, irrespective  
 274 of the number of molecules already adsorbed. Second, after saturation, the surface excess,  $\Gamma$ , will always  
 275 remain equal to the maximum surface excess,  $\Gamma_{\max}$ , and further reduction of the droplet surface area due  
 276 to evaporation will cause instantaneous desorption of the molecules back into the subsurface. In other  
 277 words, while  $\Gamma < \Gamma_{\max}$ , the surface acts as an ideal sink and when  $\Gamma = \Gamma_{\max}$ , it acts as an ideal source.  
 278 Furthermore, as mentioned before, it is assumed that the equilibrium surface excess,  $\Gamma_{\text{eq}}$ , is always equal  
 279 to the maximum surface excess,  $\Gamma_{\max}$ . Consequently, the modified boundary conditions on the surface  
 280 ( $R = 1$ ) are as follows:

$$281 \quad \begin{cases} C_i = 0, & \text{for } \Gamma < \Gamma_{\max} \\ \frac{\partial C_i}{\partial R} - \text{Pe}_i C_i - \frac{4\text{Pe}\Gamma_{\max}}{d} = 0. & \text{for } \Gamma = \Gamma_{\max} \end{cases}$$

282 The first condition is the Dirichlet boundary condition for an infinite source near the surface, and the  
 283 second condition accounts for the mass flux of the surface-active component's release into the subsurface  
 284 due to the evaporation.

285 After the solution of equation 5 at each timestep, the instantaneous mass of the component on the surface  
 286 needs to be updated accordingly. The numerical time advancement of equation 5 allows estimation of the  
 287 time required for monolayer formation and instantaneous radial concentration of trileucine inside the  
 288 droplet. Comparing this time scale to similar scales of solidification or shell formation of other excipients  
 289 and actives, it is possible to approximate the extent of surface coverage and morphology of the particles.  
 290 The use of such a predictive tool during the formulation design of inhalable particles is discussed in the  
 291 next section.



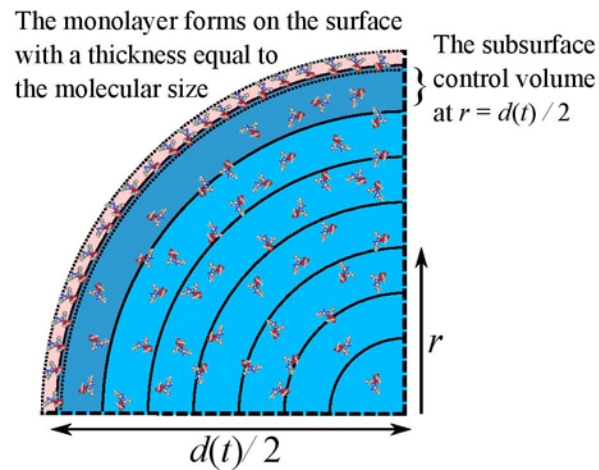
292

293

*Figure 1* The equilibrium surface tension of aqueous trileucine solutions [12] accompanied by the non-linear fit based on the

294

Szyszkowski surface equation of state.



295

296

*Figure 2* A schematic showing the discretized domains in a spherically symmetric coordinate system. The subsurface control volume is at  $r = d/2$  with a finite thickness that depends on the instantaneous droplet diameter and the number of radial nodes considered. The adsorbed monolayer has a negligible thickness equal to the molecular size of the adsorbed molecules. These adsorbed molecules do not take part in the diffusion in the bulk unless they are desorbed back into the subsurface.

297

298

299

300

#### 301 2.4.2. Phase Separation Considerations

302 One of the key properties behind the dispersibility enhancing abilities of trileucine has been hypothesized  
303 to be its surface activity [12,14,15], similar to that of other surface-active materials, such as bovine serum  
304 albumin (BSA), hydroxypropyl methylcellulose (HPMC) and poloxamer [37,42], but without much  
305 consideration given to the phase separation mechanisms involved. It was previously demonstrated that  
306 spray-dried BSA, HPMC, and poloxamer at low concentrations had high surface coverage due to  
307 monolayer surface adsorption [42]. The much larger BSA molecules (~66 kDa) had lower surface  
308 coverages compared to the smaller Poloxamer (~8-10 kDa) and HPMC molecules (~10 kDa), confirming  
309 that surface coverage was mostly controlled by surface adsorption of the surface-active molecules  
310 (discussed in the previous subsection) and not early solidification. It was also indicated that BSA and  
311 HPMC induced rugose morphologies, while poloxamer did not change the smooth morphology of the  
312 control system [42]. The lower dilatational modulus of the poloxamer solutions was reported to be the  
313 possible cause of the production of smooth particles. Among other possible explanations, the rather  
314 different aqueous solubilities of BSA (~40 mg/mL) and HPMC (~ 10 mg/mL) compared to the much  
315 higher solubility of poloxamer (very soluble) might be another cause of the difference in particle  
316 morphologies due to the earlier shell formation of the former components. The solubility of trileucine was  
317 previously altered through changes to the solution pH, resulting in different morphologies for the spray-  
318 dried particles [12]. This is difficult to explain if surface activity is the only mechanism for particle  
319 formation, because surface activity is not a strong function of pH [12]. Moreover, the low solubility of  
320 surface-active compounds was previously stated to cause early liquid-liquid phase separation [43].  
321 Consequently, to explain the rugose morphologies observed in the formulations containing trileucine, a  
322 detailed analysis of the phase separation mechanism is also required.

#### 323 **Phase Diagram of Aqueous Trileucine Solutions**

324 For crystalline shell formers, the surface concentrations are usually compared to a threshold, such as the  
325 solubility limit or a critical supersaturation at which nucleation can commence [11,18]. For a material that

326 does not crystallize during spray drying, the surface concentrations at which solidification occurs have  
327 been compared to the true density of the material [15]. However, such explanations cannot account for the  
328 early shell formation of trileucine, since an adsorbed monolayer on the surface does not increase the  
329 surface concentration to values close to the density of trileucine (more than 1000 mg/mL) and hence  
330 cannot have enough rigidity to form a solid shell without further solidification and phase separation. It is  
331 therefore hypothesized that the mechanism of shell formation and phase separation for trileucine is  
332 spinodal decomposition in the unstable regime in the free energy diagram of the aqueous solution.

333 At any given temperature, one can find the instability regime of a mixture from the free energy diagram.  
334 The instability starts at compositions at which the second derivative of the free energy with respect to  
335 concentration becomes negative. These points are usually called the spinodal points and are the  
336 boundaries of the spinodal region at which, in contrast to the metastable region, the system is unstable and  
337 readily phase separates without the presence of any kind of energy barrier or nucleation barrier [44]. In  
338 the spinodal region, the system is assumed to undergo a liquid-liquid phase separation into water-rich and  
339 water-lean states [45]. The phase diagram of aqueous trileucine solutions was estimated as explained  
340 below using the Flory-Huggins theory to help understand the actual mechanisms of phase separation.

341 Flory-Huggins theory, an extension of the regular solution theory, was originally derived for polymer  
342 solutions to account for the different molecular volumes of the solute and the solvent [46]. Taking into  
343 account the large difference in molar volumes of trileucine ( $\sim 341 \text{ cm}^3/\text{mol}$ ) and water ( $\sim 18 \text{ cm}^3/\text{mol}$ ), the  
344 Flory-Huggins theory was used to estimate the phase diagram of trileucine-water systems. A ternary  
345 Flory-Huggins procedure would be required for an optimal estimation of a water-trehalose-trileucine  
346 system. Here, the presence of trehalose in the system was neglected for simplicity.

347 Based on the Flory-Huggins theory, the free energy of mixing of a binary system,  $\Delta G_{\text{mix}}$ , at a temperature,  
348  $T$ , can be expressed as the combination of enthalpic and entropic terms as follows [46]

$$\Delta G_{\text{mix}} = nRT(x_1 \ln \phi_1 + x_2 \ln \phi_2 + x_1 \phi_2 \chi_{1,2}), \quad (6)$$

349 where  $n$  is the total number of moles in the system,  $R$  is the universal gas constant and  $x_i$  is the mole  
 350 fraction of a component.  $\phi_1 = x_1/(x_1 + Nx_2)$  and  $\phi_2 = Nx_2/(x_1 + Nx_2)$  are the volume fractions of  
 351 the solvent and the solute, respectively, while  $N$  is the ratio of the molar volumes of the solute and the  
 352 solvent. Based on this notation, subscripts 1 and 2 refer to the solvent and solute molecules, respectively,  
 353 and are not interchangeable. The interaction parameter,  $\chi_{1,2}$ , accounts for the differences in  
 354 intermolecular forces between the solvent and solute molecules and, for solutions containing polar and  
 355 hydrogen bonds, can be obtained from the Hansen solubility parameters as [47,48]

$$\chi_{1,2} = \frac{V_1}{RT} \left[ (\delta_{1,d} - \delta_{2,d})^2 + 0.25(\delta_{1,p} - \delta_{2,p})^2 + 0.25(\delta_{1,hb} - \delta_{2,hb})^2 \right], \quad (7)$$

356 in which,  $V_1$  is the molar volume of the solvent. The Hansen solubility parameters  $\delta_{i,d}$ ,  $\delta_{i,p}$  and  $\delta_{i,hb}$   
 357 account for the dispersion forces, polar forces, and hydrogen bonding interactions, respectively. The  
 358 Hansen solubility parameters of trileucine were calculated using two different group contribution methods  
 359 of Hoy and Van Krevelen [49]. The average value of the solubility parameters obtained from these two  
 360 methods was used in this study. The obtained values were  $\delta_{tl,d} = 15.8 \text{ MPa}^{1/2}$ ,  $\delta_{tl,p} = 7.8 \text{ MPa}^{1/2}$  and  
 361  $\delta_{tl,hb} = 9.6 \text{ MPa}^{1/2}$ . For water, the available Hansen solubility parameters,  $\delta_{w,d} = 15.5 \text{ MPa}^{1/2}$ ,  $\delta_{w,p} =$   
 362  $16.0 \text{ MPa}^{1/2}$  and  $\delta_{w,hb} = 42.3 \text{ MPa}^{1/2}$  were used [48]. The interaction parameter of the trileucine-water  
 363 system was then calculated to be  $615.3/T$ , with the temperature in Kelvin. The Gibbs free energy of  
 364 mixing was obtained for this binary system at any given temperature and composition. The solution of  
 365  $\partial^2 \Delta G_{\text{mix}} / \partial x_1^2 = 0$  resulted in the determination of the spinodal points.

366 The spinodal curves for this binary system versus trileucine concentration are shown in Figure 3 between  
 367  $5 \text{ }^\circ\text{C}$  and  $100 \text{ }^\circ\text{C}$ . At a solution temperature of  $25 \text{ }^\circ\text{C}$ , the trileucine mole fraction at the left spinodal point  
 368 was calculated to be about 0.09%, corresponding to a concentration of  $C_{\text{sp,Leu3}} = 18 \text{ mg/mL}$ . Based on  
 369 this simplified model, it can be assumed that upon reaching this concentration, trileucine undergoes  
 370 spontaneous liquid-liquid separation into water-rich and trileucine-rich phases. During spray drying, the  
 371 phase separation would most likely start near the droplet surface due to the higher local concentration (in

372 the subsurface domain due to the surface recession) and the presence of the adsorbed monolayer at the  
 373 interface. This kind of liquid-liquid phase separation was previously put forward as an explanation for the  
 374 core-shell structure of atmospheric aerosols containing surface-active organic compounds with low  
 375 aqueous solubility [43,50].

### 376 **Prediction of the Onset of Phase Separation**

377 As the liquid-liquid phase separation and spinodal decomposition are a bulk process with a higher  
 378 probability of separation near the droplet surface, to predict the onset of phase separation the subsurface  
 379 concentration can be compared to the spinodal concentration,  $C_{sp,Leu3} = 18 \text{ mg/mL}$ . The subsurface  
 380 concentration can either be calculated from the solution of equation 5 or obtained by using a simplified  
 381 method as follows. After reaching a saturated surface monolayer,  $\Gamma(t) = \Gamma_{max}$ , and assuming the number  
 382 of adsorbed molecules into the monolayer is small relative to the molecules in the bulk, the subsurface  
 383 concentration of the  $i$ th component can be obtained from the steady-state surface enrichment value based  
 384 on what is known as the “VFL” model [18,19],

$$E_{s,i} = \frac{C_{s,i}}{C_{m,i}} \approx 1 + \frac{Pe_i}{5} + \frac{Pe_i^2}{100} - \frac{Pe_i^3}{4000} \quad \text{for } Pe_i = \frac{\kappa}{8D_i} < 20, \quad (8)$$

385 where  $C_{s,i}$  and  $C_{m,i}$  are the instantaneous subsurface and mean concentrations, respectively, excluding the  
 386 number of adsorbed molecules in the monolayer. The mean concentration of component  $i$  can be obtained  
 387 from

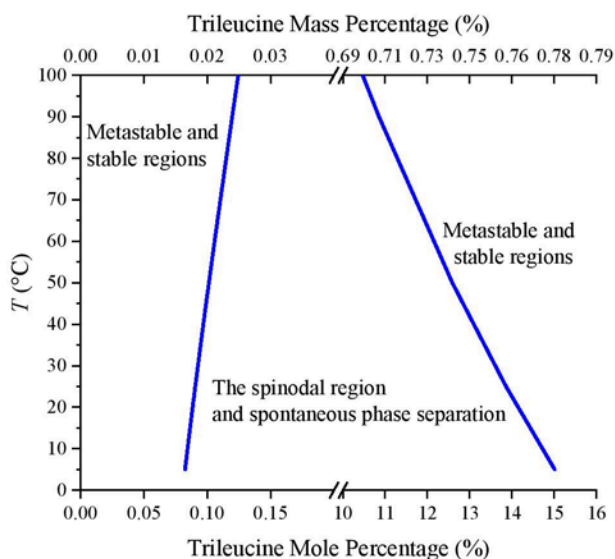
$$C_{m,i} = C_{0,i}(1 - \tau)^{-3/2} - \frac{6\Gamma_{max}}{d_0}(1 - \tau)^{-1/2}, \quad (9)$$

388 where  $C_{0,i}$  is the initial feed concentration of this component and  $\tau = t/t_d$  is the dimensionless time,  
 389 while  $t_d = d_0^2/\kappa$  is the drying time of the droplet and  $d_0$  is the initial droplet diameter. In equation 9, the  
 390 second term on the right was added to account for the amount of material adsorbed onto the interface and  
 391 is negligible for non-surface-active molecules. It is important to note that equations 8 and 9 give  
 392 reasonable results only after some time has passed, since the monolayer has been saturated. Assuming the

393  $\frac{6\Gamma_{\max}}{d_0}$  term is negligible, the dimensionless time at which spinodal decomposition commences for the  $i$ th  
 394 component can be obtained from the combination of equations 8 and 9 as

$$\tau_{sp,i} = t_{sp,i}/t_d = 1 - \left( \frac{C_{0,i}E_{s,i}}{C_{sp,i}} \right)^{\frac{2}{3}}. \quad (10)$$

395 Where the assumption in arriving at equation 10 does not hold, for example, in cases of small initial  
 396 droplets or droplets with low initial solute concentrations, equation 5 should be solved numerically to find  
 397 the respective time for the initiation of phase separation. During formulation design, equation 10 can be  
 398 compared to similar timescales such as time to reach saturation for crystallizing components or time to  
 399 reach true density for highly soluble amorphous components in order to better predict the particle  
 400 formation processes, if relevant, for other competing components present in the system [15].



401  
 402 *Figure 3* The Spinodal curve of the trileucine-water system obtained from the Flory-Huggins theory. A transition into the  
 403 spinodal region will induce spontaneous liquid-liquid separation into water-rich and water-lean phases.

404

### 3. Results and Discussions

#### 3.1. Single-Particle Measurements Using the CK-EDB Instrument

The time of shell formation and solidification, as well as the instantaneous morphology of the droplets containing trileucine and trehalose, was estimated using the CK-EDB instrument. The evaporation histories of one sample droplet for each case are shown in Figure 4. The approximate instantaneous particle morphologies are also color-coded, with blue representing optically spherical and homogenous, black representing spherical but with internal inclusions, red representing a core-shell morphology, and purple representing non-spherical. The measurement of the diameter is reliable as long as the particle maintains optical homogeneity (blue); the size estimated when the particle is non-spherical and optically inhomogeneous should not be considered accurate. For both the aqueous-trileucine and aqueous-trileucine-trehalose solution droplets, the linear portion of the  $d^2$  vs time plots (the constant evaporation rate period) decreases with an increase in trileucine content, pointing to earlier shell formation that occurs at larger particle diameters. For all cases, the droplets were initially spherical during the constant-rate evaporation period, with a transition to non-spherical particles. For lower trileucine concentrations, this transition regime was rather sharp and sudden; with an increase of trileucine content, the transition was more gradual, with the appearance of a mixture of core-shell and spherical-with-inclusion morphologies before the final phase change. In such cases, the phase-separated domains were likely large enough to be discernible by light scattering and detected by the algorithm used for morphology detection. The core-shell morphology points to the preferential phase-separation on the droplet surface, while the appearance of individual domains (inclusions) inside the droplets might be due to additional spinodal decomposition inside the evaporating droplet.

The quantification of the data obtained from the single-particle experiments was achieved by the determination of the time and diameter at which the evaporation rates were no longer constant and a deviation from the  $d^2$ -law was observed [18]. Henceforth, this instance will be called the critical point of shell formation or solidification, denoted by the subscript  $c$  and corresponding to the approximate time at

430 which a sufficiently viscous shell forms to hinder the evaporation of the remaining water in the droplets.  
431 The normalized critical diameters,  $d_c/d_0$ , and critical times,  $\tau_c = t_c/t_d$ , of the trileucine and  
432 trileucine/trehalose particles are shown in Figure 5. These data are shown versus both the initial trileucine  
433 concentration,  $C_{0,\text{Leu3}}$ , and the respective initial trileucine saturation,  $S_{0,\text{Leu3}}$ , multiplied by the steady-  
434 state surface enrichment of trileucine,  $E_s$ . The steady-state surface enrichment, which is a function of the  
435 Péclet number, accounts for the amount of material accumulating on the droplet surface due to the  
436 recession of the droplet surface alone [15,18]. The advantage of such representation of the trileucine  
437 content will be explained later. For both the trileucine and the trileucine/trehalose cases, the critical  
438 diameter increased and the critical time decreased with an increase to trileucine content, resulting in  
439 particles with lower densities. This observation supports the hypothesis that the precipitation and the  
440 subsequent shell formation of trileucine are initiated upon achieving a certain critical concentration that  
441 leads to spinodal decomposition. It is also evident that the neat trileucine systems reached the critical shell  
442 formation state at a slightly later stage and at smaller diameters compared to the trileucine/trehalose  
443 systems, perhaps because of the higher total concentration and viscosity in the latter systems. The minor  
444 difference between the trileucine and the trileucine/trehalose systems means that trehalose does not  
445 interfere considerably with the phase separation and shell formation of trileucine. This justifies the use of  
446 a binary phase diagram for water and trileucine in the presence of trehalose. A non-linear fit to the  
447 normalized time of shell formation of trileucine gives

$$\tau_{c,\text{Leu3}} = t_{c,\text{Leu3}}/t_d = 1 - 0.24(E_s S_{0,\text{Leu3}})^{2/3}, \quad (11)$$

448 where, as stated before,  $E_s$  is the steady-state surface enrichment obtained from equation 8 and  $S_{0,\text{Leu3}}$  is  
449 the initial trileucine saturation. This equation resembles the relationships obtained from the mass balance  
450 consideration inside the droplet for other thresholds, such as the time to reach saturation and the time to  
451 reach the true density of a component [15], and can be used to predict the approximate time of shell  
452 formation of trileucine. The data used in arriving at equation 11 were obtained for relatively large droplets  
453 ( $d_0 \cong 50 \mu\text{m}$ ), and their accuracy for smaller atomized droplets, such as those encountered in spray

454 drying of inhalable particles, cannot be verified directly. Nevertheless, the size dependency of the time for  
455 shell formation is expected to be more considerable for crystallizing systems that need to overcome an  
456 energy barrier and undergo nucleation and crystal growth [11]. Spinodal decomposition is expected to be  
457 faster and hence the use of equation 11 for smaller droplet sizes appears reasonable.

458 The normalized time for trileucine to reach a concentration of  $C_{sp,Leu3} = 18$  mg/mL at the subsurface  
459 domain was predicted using equation 10 and is shown as the grey line in Figure 5. Similar results were  
460 obtained via the numerical solution of equation 5 because for the large droplets encountered in the EDB  
461 experiments, the monolayer formation happened much earlier relative to the droplet lifetime (this will be  
462 discussed later). As expected, the subsurface concentration reached the predicted spinodal point earlier  
463 than the critical shell formation time measured via the single-particle measurements. Upon reaching the  
464 spinodal point, the trileucine molecules in the bulk separate into a water-rich phase and a water-lean  
465 phase quickly, most likely near the surface. The water-lean domains accumulated near the surface are  
466 expected to undergo further water loss due to the continuing evaporation, until the viscosity of the glassy  
467 phase is large enough for a shell to form and fold upon further shrinkage and evaporation.

468 After a while, the instrument detected a drop in evaporation rates and different morphologies. This time  
469 delay between  $\tau_{sp,Leu3}$  and  $\tau_c$  is shown as the area between the measured and predicted curves in Figure  
470 5. The delay increased with an increase in initial trileucine content, likely because phase separation  
471 happened at a larger droplet diameter at higher trileucine contents, and it takes more time to make a  
472 viscous shell that can arrest droplet shrinkage on the larger droplets.

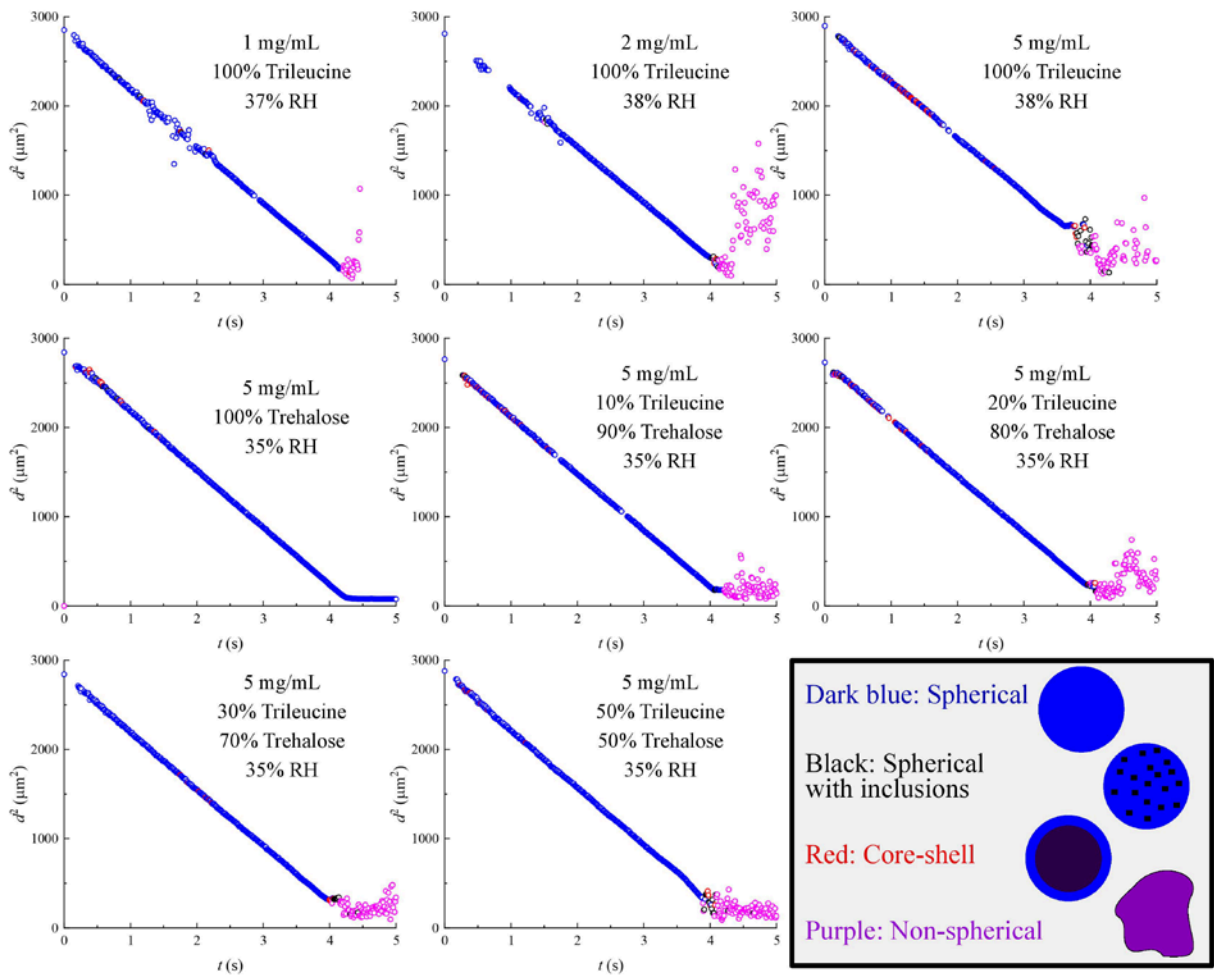
473 To also investigate the precipitation behavior of the system, the bulk concentration of trileucine at the  
474 critical shell formation,  $C_{c,Leu3}$ , obtained from a simple mass balance equation and the measured  $d_c$  [11],  
475 versus the initial trileucine concentration,  $C_{0,Leu3}$ , is shown in Figure 6. In all cases, the bulk critical  
476 concentration was measured to be larger than the previously calculated spinodal point of trileucine in

477 water (~18 mg/mL). This also agrees with our assumption of spinodal decomposition of trileucine during  
478 drying and the ensuing delay time as discussed above.

479 For the neat trileucine systems,  $C_{c,Leu3}$  is slightly lower at higher trileucine concentrations. This agrees  
480 with the previous observations because for the cases of neat trileucine a higher  $C_{0,Leu3}$  means reaching the  
481 spinodal point earlier and at a larger droplet diameter and hence at a smaller bulk concentration. This  
482 behavior is reversed for the trileucine/trehalose systems, whose critical bulk concentrations are always  
483 lower at similar neat trileucine feed concentrations. This difference could be explained by the possible  
484 coprecipitation of trileucine and trehalose. For a leucine/trehalose system, such a trend was not observed  
485 due to the independent crystallization and shell formation of leucine [11]. To further assess the validity of  
486 this hypothesis of coprecipitation of trileucine and trehalose, the surface concentration of trehalose at the  
487 time that trileucine reached its spinodal point was estimated using the VFL method. This showed a  
488 decrease from around 160 mg/mL to 20 mg/mL when the trileucine fraction was increased from 10% to  
489 50% while the total feed concentration was kept constant at 5 mg/mL. These values were larger than the  
490 spinodal concentration of trileucine (~18 mg/mL). Hence, it could be expected that both of the phase-  
491 separated domains had some trehalose content, with the water-rich phases possibly having a higher  
492 trehalose content than the trileucine-rich phases. The ability of trileucine to coprecipitate with other  
493 components, along with its high glass transition temperature, ~104 °C [12], might be contributing to its  
494 superior performance in stabilizing biologics [16,17].

495 The critical bulk concentration of trehalose,  $C_{c,treh}$ , obtained from neat trehalose droplets was previously  
496 measured and was also confirmed from the data in Figure 4 to be around  $830 \pm 15$  mg/mL [11]. This  
497 result indicates that trehalose by itself is expected to undergo a rapid rise in viscosity and glass formation  
498 upon reaching this bulk concentration.

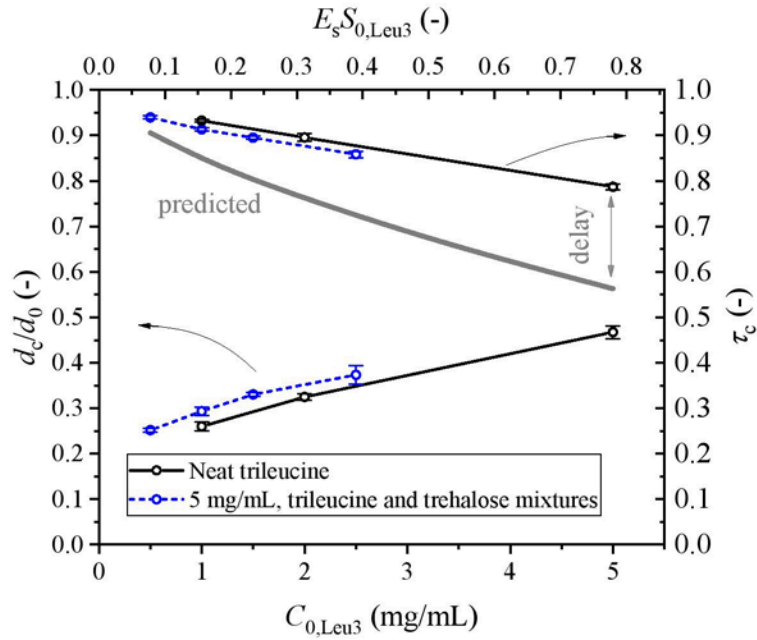
499



500

501  
502  
503

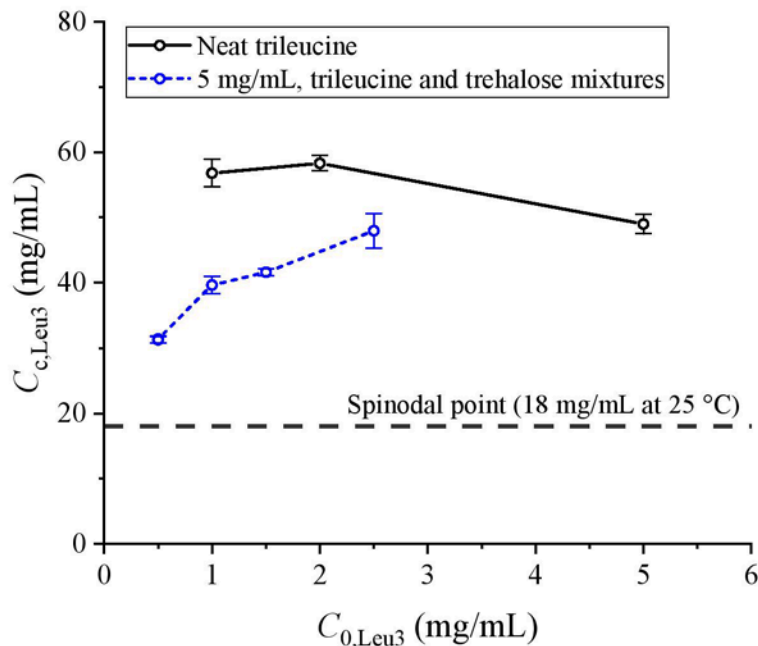
Figure 4 Sample evaporation histories of the formulations studied with the CK-EDB instrument. The drying temperature was 20 °C for all cases. The data points are color-coded with the approximated morphologies as explained at the bottom right. The measured sizes are reliable only for optically spherical particles (blue).



504

505 *Figure 5* The normalized critical diameters (bottom curves) and times of shell formation and solidification (top curves) for the  
 506 trileucine and trileucine/trehalose systems obtained from the deviation from the  $d^2$ -law in the CK-EDB measurements versus the  
 507 initial trileucine concentration at the bottom and the initial trileucine saturation multiplied by the steady-state surface enrichment  
 508 at the top. The error bars represent one standard deviation of the multiple droplets studied per case. The drying temperature was  
 509 20 °C for all cases. The initial droplet diameters were approximately 50  $\mu\text{m}$ . The grey line is the predicted time for spinodal  
 510 decomposition to commence obtained from equation 10.

511



512

513 *Figure 6* The apparent bulk concentration of trileucine at the critical time of shell formation obtained from the CK-EDB  
 514 measurements. The drying temperature was 20 °C for all cases. The initial droplet diameters were approximately 50 μm. Here,  
 515 the bulk concentration is obtained from the total amount of trileucine in the droplet divided by the droplet diameter at shell  
 516 formation; hence it includes the amount of material adsorbed onto the surface too. The error bars correspond to the standard  
 517 deviation of three measurements per case.

518

### 519 3.2. Monodisperse Particles from the Droplet Chain Instrument

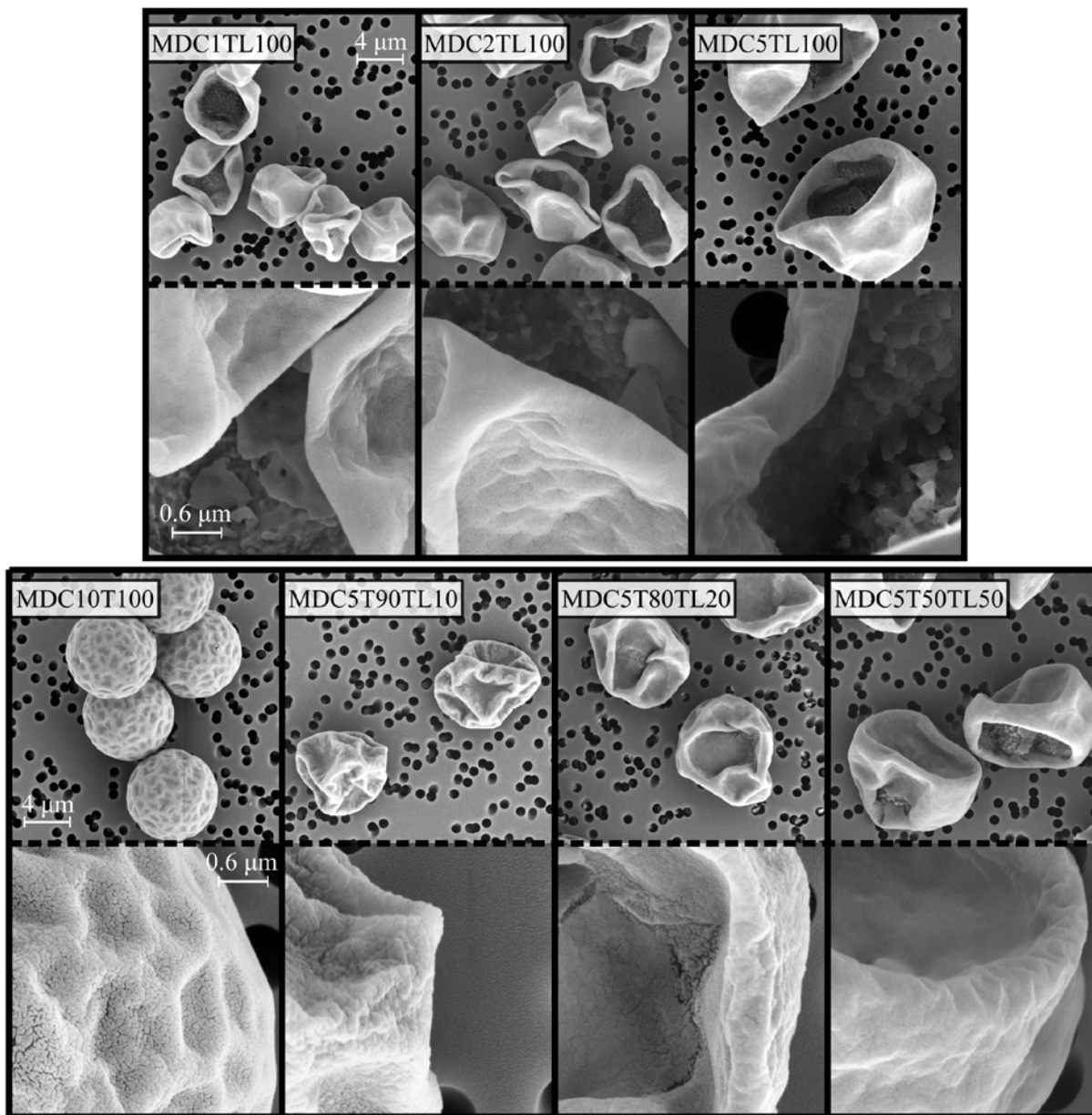
520 The SEM micrographs of monodisperse particles generated using the droplet chain instrument are shown  
 521 in Figure 7. As mentioned earlier, the formulations studied using the droplet chain instrument (seen in  
 522 Table 2) were chosen to represent the systems measured via the CK-EDB instrument for which the final  
 523 dried particles cannot be collected. Two different magnifications are provided for each sample to study  
 524 both the micro- and nano-scale morphologies of the particles. In agreement with the observations from the  
 525 CK-EDB, the particles were bigger and less dense at higher trileucine feed concentrations for both the  
 526 trileucine and the trileucine/trehalose systems. A folded shell can be observed for all particles that contain  
 527 trileucine, which is evidence of the presence of a pliable skin that can wrinkle and fold and eventually dry  
 528 into a shell. The nanostructure at the surfaces of the trileucine particles was smooth, possibly due to the  
 529 monolayer formation at the droplet interface and the absence of any crystals. It can also be observed that

530 the inside of the particles is visible due to the presence of a hole for all three trileucine cases and the last  
531 case of the trileucine/trehalose systems with the highest trileucine fraction. These holes are possibly  
532 caused by the rupture of the thin-shelled particles during drying. As seen in the ultra-magnified  
533 micrographs, the morphology of the interior of these particles is completely different from the surface  
534 morphology.

535 The measured normalized particle diameters,  $d_p/d_0$ , are shown in Figure 8. At similar compositions, the  
536 normalized diameters of the dried particles are slightly smaller than the normalized critical diameters of  
537 shell formation obtained from the CK-EDB instrument (refer to Figure 5). This is because after shell  
538 formation the particles can still lose their water content and shrink, but at a slower rate. The gradual  
539 increase of the particle diameters with an increase in trileucine content is also visible. The particle  
540 densities,  $\rho_p$ , also shown in Figure 8, were obtained from the equation for the mass balance of the  
541 involatile components as [15]:

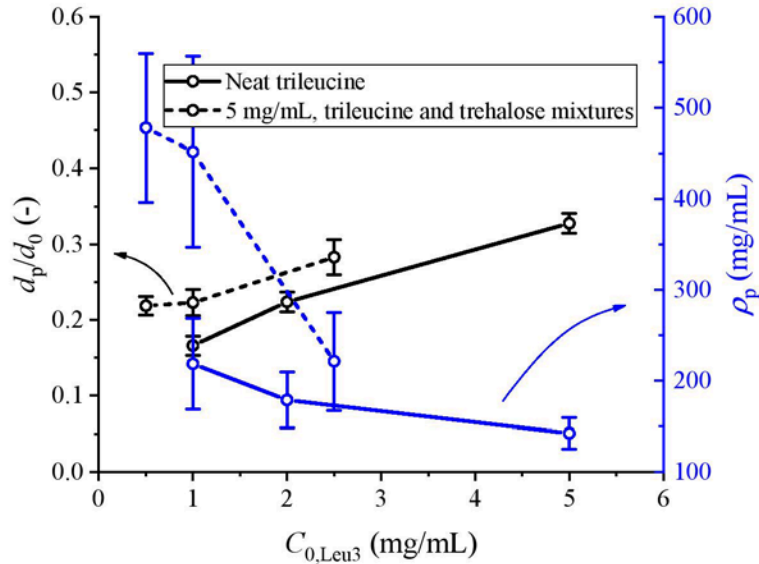
$$\rho_p = C_{0,t}(d_0/d_p)^3, \quad (12)$$

542 where  $C_{0,t}$  is the total feed concentration. The particle density obtained from this equation gives an  
543 envelope density for which the internal and external voids are also considered in the volume. The  
544 inclusion of only 10% trileucine (0.5 mg/mL) decreased the particle density to about 500 mg/mL, while  
545 the density of neat trehalose particles is measured to be larger than 1500 mg/mL from the MDC10T100  
546 system. The particle densities decreased further with an increase to the trileucine content. Moreover, the  
547 particle densities of trileucine/trehalose systems were larger than those of neat trileucine cases at the same  
548 conditions. An increasing amount of void space is opened up as the trileucine content is increased,  
549 creating the potential to produce particles with very low density. Elsewhere, it has been shown that at  
550 very small concentrations, trileucine does not change the morphology of trehalose-containing particles,  
551 while the particles' dispersibility already increases due to the adsorbed surface monolayer [13]. These  
552 observations show that this system is suitable for both high- and low-density particle design targets with  
553 superior aerosol performance.



554

555 *Figure 7* The micrographs of the monodisperse particles collected from the droplet chain instrument at two different  
 556 magnifications. The drying temperature was 20 °C for all cases. Each scale bar applies to its respective row. The initial droplet  
 557 diameters were approximately 40 μm.



558

559 *Figure 8* The normalized particle diameters (shown in black) and the particle densities (shown in blue) obtained from the  
 560 monodisperse droplet chain instrument. The error bars represent one standard deviation. The drying temperature was 20 °C for all  
 561 cases and the initial droplet diameters were approximately 40  $\mu\text{m}$ .

562

### 563 3.3. Spray-Dried Powders

564 The spray-dried powders were also studied in order to broaden the scope of analysis to include conditions  
 565 representative of actual industrial settings, in particular the spatially varying parameters inside the spray  
 566 plume, such as temperature, relative humidity, and the smaller initial sizes of the polydisperse atomized  
 567 droplets. It was especially of interest to determine whether the findings obtained from the larger droplets  
 568 at lower drying temperatures could be generalized to practical industrial conditions.

569 The micrographs of the spray-dried trileucine/trehalose particles are shown in Figure 9. As with the  
 570 monodisperse particles, increasing the trileucine content caused the particles to become larger and less  
 571 dense and to develop rugose surfaces. Compared to the trehalose particles, the addition of only 2%  
 572 trileucine (1 mg/mL) caused considerable morphological differences due to early liquid-liquid phase  
 573 separation. Compared to the spray-dried leucine/trehalose particles, which had a variety of different  
 574 particle morphologies for different particle sizes (or different initial droplet sizes) of the same batch [11],  
 575 the trileucine/trehalose particles have similar general morphologies irrespective of their sizes. This

576 difference in behavior is further evidence for the different phase separation behaviors of leucine  
577 (nucleation and crystal growth with an energy barrier) and trileucine (spinodal decomposition near the  
578 surface) during spray drying.

579 Raman spectroscopy measurements (not shown) confirmed that both the trehalose and trileucine  
580 components were completely amorphous in all of the spray-dried batches [16,17], refuting the possibility  
581 of early nucleation and crystal growth as the origins of trileucine shell formation.

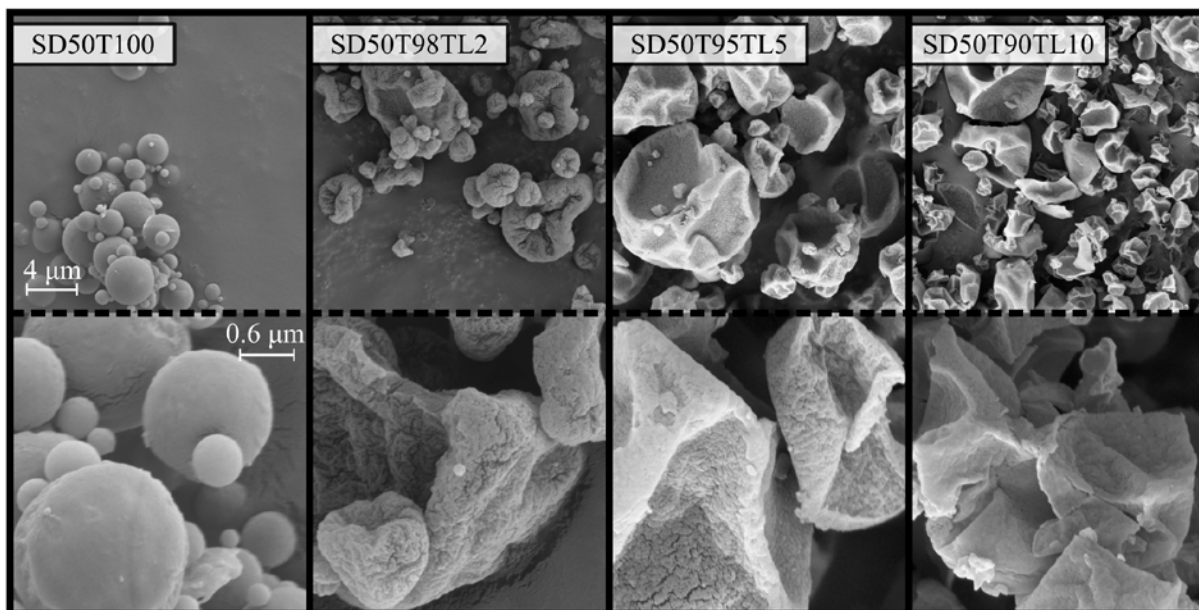
582 The surface compositions of the spray-dried particles are shown in Figure 10. In these 8-bit RGB images  
583 obtained from the TOF-SIMS instrument, the blue and red channels were reserved for the signal strengths  
584 of trehalose and trileucine, respectively. The pixel-average surface compositions of the powders as a  
585 whole, small ( $d < 1 \mu\text{m}$ ), medium ( $1 < d < 3 \mu\text{m}$ ), and large particles ( $d > 3 \mu\text{m}$ ) are shown in Figure  
586 11. It is seen that the powders exhibit more trileucine on the surface at higher trileucine feed fractions.

587 The surface coverage of trileucine increased from ~70% w/w to ~92% w/w through an increase to its feed  
588 fraction from 2% w/w to 10% w/w. It is observed that nearly complete surface enrichment of trileucine  
589 (nearly 40-fold compared to the bulk) is achieved by the addition of small quantities of this shell former.

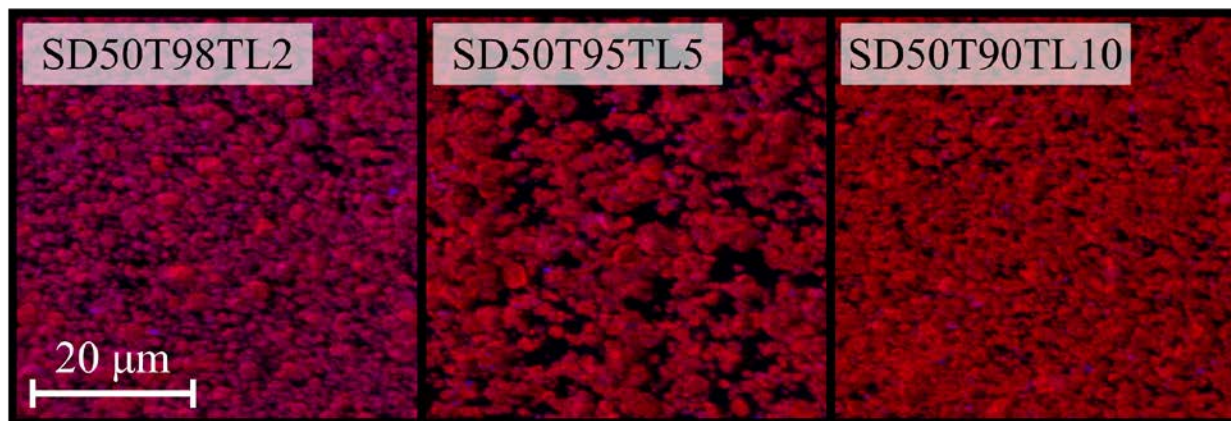
590 It is interesting to note that previous TOF-SIMS measurements of leucine/trehalose particles showed that  
591 the addition of different mass fractions of leucine ranging from 10 to 40% resulted in less than 3-fold  
592 surface enrichment compared to the bulk fractions [11]. Considering the probe depth of the TOF-SIMS  
593 instrument (~3-5 nm), the extremely high surface coverage of trileucine is likely due to the presence of  
594 the saturated monolayer (the diameter of a trileucine molecule is about 0.9 nm) as well as the liquid-liquid  
595 phase separation due to spinodal decomposition with low trehalose content in the trileucine-rich phase.

596 Compared to leucine/trehalose particles [11], the trileucine/trehalose particles are similar across different  
597 particle sizes, pointing yet again to the different shell formation mechanisms of leucine and trileucine. It  
598 was observed that the particles with the smallest trileucine content (SD50T98TL2) had slightly different  
599 surface compositions for different particle sizes, with smaller particles having less trileucine on the  
600 surface than the larger particles. This behavior was not as discernible at higher trileucine fractions. The

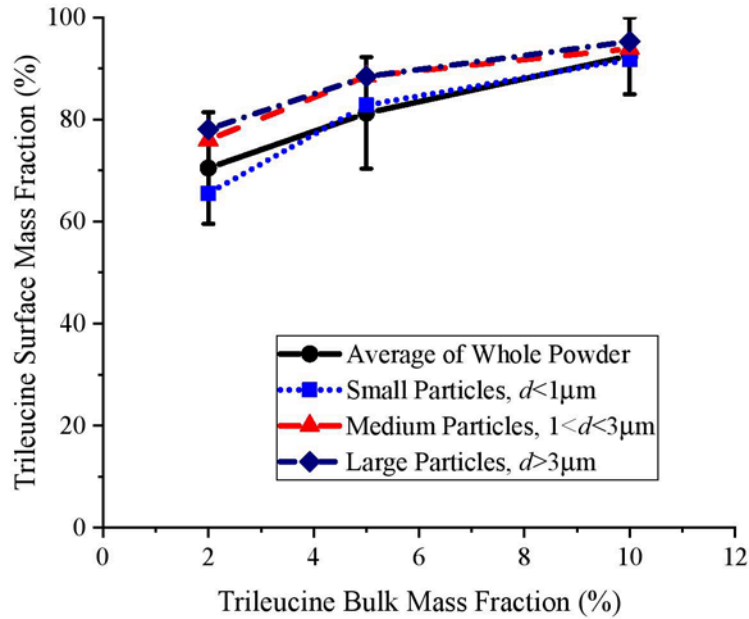
601 monolayer surface adsorption due to the trileucine surface activity is likely responsible for this difference  
602 in surface compositions as the thickness of the monolayer,  $\sim 1$  nm, comprises more than 20% of the probe  
603 depth of the TOF-SIMS instrument. This in turn means that a non-saturated monolayer ( $\Gamma < \Gamma_{\max}$ ) on the  
604 smaller particles would affect the measured surface coverage slightly.



605  
606 *Figure 9* The micrographs of the spray-dried trileucine/trehalose particles at two different magnifications. The drying temperature  
607 was 75 °C for all cases. Each scale bar applies to its respective row.



608  
609 *Figure 10* The TOF-SIMS 8-bit RGB images of the spray-dried trileucine/trehalose particles. The red and blue channels represent  
610 the trileucine and trehalose surface compositions, respectively. The drying temperature was 75 °C for all cases.



611

612 *Figure 11* The pixel-average surface compositions of the whole powder, small, medium, and large spray-dried particles. The  
 613 drying temperature was 75 °C for all cases. The error bars represent the standard deviation.

614

### 615 3.4. Implications for Formulation and Process Design via Particle Engineering for 616 Surface-Active Materials

617 As discussed above, the surface adsorption of trileucine plays an important role in its higher surface  
 618 enrichment in spray-dried particles. Hence, the kinetics of the monolayer formation should be studied in  
 619 more depth for a successful particle design of systems containing at least one surface-active component.

620 The adsorption of surface-active materials on the droplet interface was previously approximated using  
 621 equation 4 [38], which was originally obtained for the adsorption of surfactants on the interface of a semi-  
 622 infinite medium [40]. The use of this relationship does not account for the depletion of the solute  
 623 molecules in small atomized droplets (due to the large surface-to-volume ratio of a small sphere), nor  
 624 does it account for the effect of the receding droplet surface due to evaporation. To explain these effects,  
 625 equation 5 was solved in conjunction with the appropriate boundary conditions for trileucine at different  
 626 initial droplet diameters, feed concentrations, and drying temperatures. The bulk concentration,

627 subsurface concentration, and adsorbed surface excess of a sample case versus time are shown in Figure  
628 12 (a). The initial droplet diameter was 8  $\mu\text{m}$ , trileucine feed concentration was 1 mg/mL and the drying  
629 temperature was 75  $^{\circ}\text{C}$ , imitating the conditions of the SD50T98TL2 spray-dried case. Until a certain  
630 point in time,  $t_{\Gamma}$ , at which the maximum surface excess of 0.99 mg/m<sup>2</sup> was reached, the subsurface  
631 concentration was zero, while the bulk concentration decreased due to the surface adsorption. Upon  
632 reaching the maximum surface excess at  $t_{\Gamma}$ , the enforced boundary conditions were switched, and  
633 desorption from the interface into the subsurface commenced due to the decreasing surface area and the  
634 fact that the surface excess cannot be increased past the maximum value,  $\Gamma_{\text{max}}$ . Eventually, the subsurface  
635 concentration increased similarly to the ordinary particle formation predictions explained elsewhere  
636 [19,24]. These behaviors can also be seen from the internal radial concentration distributions of the same  
637 droplet at different time points during the evaporation period shown in Figure 12 (b).

638 The time to reach the maximum surface excess,  $t_{\Gamma}$ , for different trileucine feed concentrations as a  
639 function of the initial droplet diameter obtained from the numerical simulations is shown in Figure 13 for  
640 drying temperatures of 20  $^{\circ}\text{C}$  and 75  $^{\circ}\text{C}$ . The times required to reach surface saturation obtained from  
641 equation 4 (semi-infinite volume case) are also shown as the horizontal lines for each respective feed  
642 concentration; surprisingly, these are not identical for the same concentration at different temperatures.  
643 The reason is the lower aqueous viscosity at the higher wet-bulb temperature and hence the higher  
644 trileucine diffusion coefficient for the drying temperature of 75  $^{\circ}\text{C}$  compared to 20  $^{\circ}\text{C}$ .

645 Also shown in Figure 13 as grey dashed lines are the drying times,  $t_d$ , of the droplets with different  
646 diameters. The numerical results converge to those obtained from equation 4 at larger initial droplet  
647 diameters, but the results deviate for smaller diameters and feed concentrations due to the shorter drying  
648 times of the small droplets. Considering only the horizontal lines obtained from equation 4, any case that  
649 has an initial droplet diameter to the left of the intersection of the respective line and the  $t_d$  line would not  
650 have enough time to form a monolayer on the droplet surface. For example, the drying time of a droplet  
651 with an initial diameter of 2  $\mu\text{m}$  and a trileucine concentration of 0.5 mg/mL dried at 75  $^{\circ}\text{C}$  is less than

652 the time required to reach the maximum surface excess obtained from equation 4. However, as seen from  
653 the full numerical results, the reality is different. Even though the droplet's lifetime is less than the time  
654 required for surface saturation obtained from the simple equation, there will still be a fully adsorbed  
655 monolayer near the end of the drying process due to droplet shrinkage. It is for this reason that in Figure  
656 13 the numerical results are tangent to the  $t_d$  curves for smaller initial droplet diameters and for the cases  
657 with low trileucine concentrations.

658 It is also observed that at the lower drying temperature of 20 °C, the curves for the trileucine feed  
659 concentrations of 0.1, 0.5, and 1 mg/mL have local maxima above their respective horizontal lines. The  
660 longer times required for monolayer formation for these low-concentration cases are due to the depletion  
661 of the solute molecules in the bulk at smaller initial droplet diameters (higher surface-to-volume ratio). At  
662 these conditions, the droplet shrinkage due to evaporation is not fast enough to maintain the bulk  
663 concentration while the solute material is being adsorbed onto the interface. At larger initial droplet  
664 diameters and smaller surface-to-volume ratios, the curves eventually converge with the horizontal lines.  
665 This behavior was not observed for the droplets evaporating at 75 °C, and the curves converged with the  
666 horizontal lines monotonically due to the fast evaporation of the droplets. Importantly, it can be  
667 concluded that for droplets typically encountered in industrial spray dryers (i.e.  $d > 7 \mu\text{m}$ ) and typical  
668 drying gas conditions (the 75 °C plot), the time to form a saturated monolayer is very fast compared to the  
669 droplet lifetime, except in cases of very low initial trileucine concentrations.

670 In the presence of other excipients or actives another condition needs to be considered for particle design:  
671 for a saturated trileucine monolayer to form, the calculated  $t_\Gamma$  needs to be shorter than the shortest time of  
672 solidification of other components. Also, it can now be concluded that the shell formation and  
673 solidification of trileucine is a sequential process with monolayer formation being the first stage (at  $\tau_\Gamma$   
674 from Figure 13), followed by spinodal decomposition (at  $\tau_{\text{sp,Leu3}}$  from equation 10), and then the final  
675 period of the formation of a rigid shell on the surface of the droplet (at  $\tau_{\text{c,Leu3}}$  from equation 11). The  
676 critical solidification times of other components and active ingredients can now be compared to these

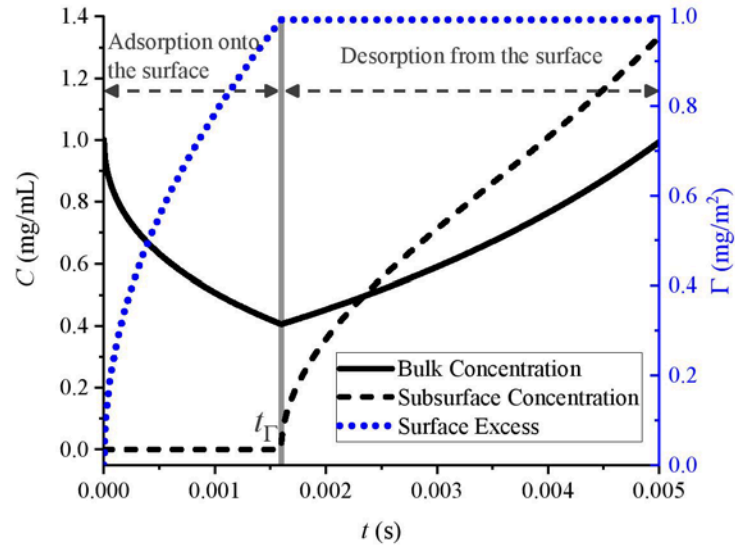
677 values during formulation design. For the trileucine/trehalose platform studied in this article, the critical  
678 time of solidification for trehalose,  $\tau_{c,Treh}$ , is assumed to be the time at which it reaches a bulk  
679 concentration of 830 mg/mL and is obtained from

$$\tau_{c,Treh} = 1 - \left( \frac{C_{0,Treh}}{830 \text{ mg/mL}} \right)^{2/3}, \quad (13)$$

680 in which  $C_{0,Treh}$  is the initial feed concentration of trehalose in mg/mL. For trehalose, the bulk  
681 concentration can be used as a threshold in particle formation, as its Péclet number is small enough to  
682 give a surface enrichment of close to 1 at these drying temperatures [11]. As an example, the time points  
683 of interest for three different trileucine/trehalose systems analogous to the spray-dried formulations were  
684 calculated and are reported in Figure 14. It is observed that for all cases  $\tau_T$  was much smaller than the  
685 solidification time of trehalose,  $\tau_{c,Treh}$ . But for the first system with 2% w/w trileucine,  $\tau_T$  was relatively  
686 close in magnitude to  $\tau_{c,Treh}$  for small initial droplet diameters. This difference increased for greater  
687 trileucine fractions. This fact is assumed to be one of the reasons for the relatively dissimilar surface  
688 compositions among different particle sizes of the SD50T98TL2 system as shown in Figure 10. In the  
689 first case with 2% w/w trileucine,  $\tau_{sp,Leu3}$  was close to  $\tau_{c,Treh}$  explaining possible solidification of  
690 trileucine and trehalose at similar times. In the systems with higher trileucine fractions in Figure 14, it is  
691 predicted that the spinodal decomposition of trileucine starts long before the solidification of trehalose.  
692 Note that in the simplified discussion here, the liquid-liquid phase separation of the ternary system of  
693 trileucine and trehalose with water is not considered. Based on the plots shown in Figure 14, trileucine is  
694 expected to act as a strong dispersibility enhancer for all three systems, because a saturated monolayer  
695 could be formed on the droplet surface before other components could interfere with the surface  
696 adsorption. The presence of this monolayer is responsible for reducing the surface energy of the dried  
697 particles and in turn increasing the dispersion properties of the resulting powders. The increase of  
698 trileucine fractions from 2% w/w to 10% w/w is expected to cause a thicker trileucine shell on the surface

699 that might not be necessary to maintain the dispersibility enhancement but that can greatly decrease the  
700 particle density if the goal of the design process is producing low-density particles.

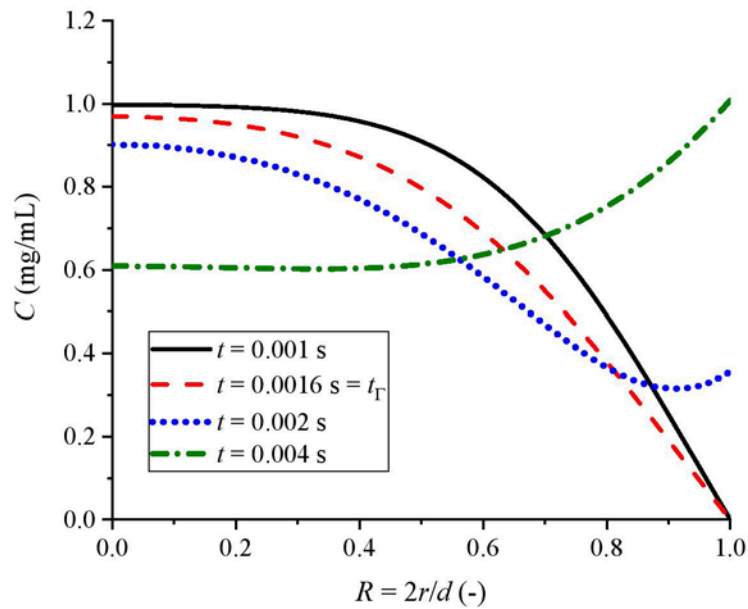
701 Using a similar methodology, a formulator can design a system composed of many excipients and active  
702 ingredients. It should be noted here that multiple surface-active components in the same system are  
703 expected to interfere with each other's surface adsorption. In that case, the methodology proposed for the  
704 prediction of surface adsorption of the components in such systems would need to be modified.



705

706

(a)

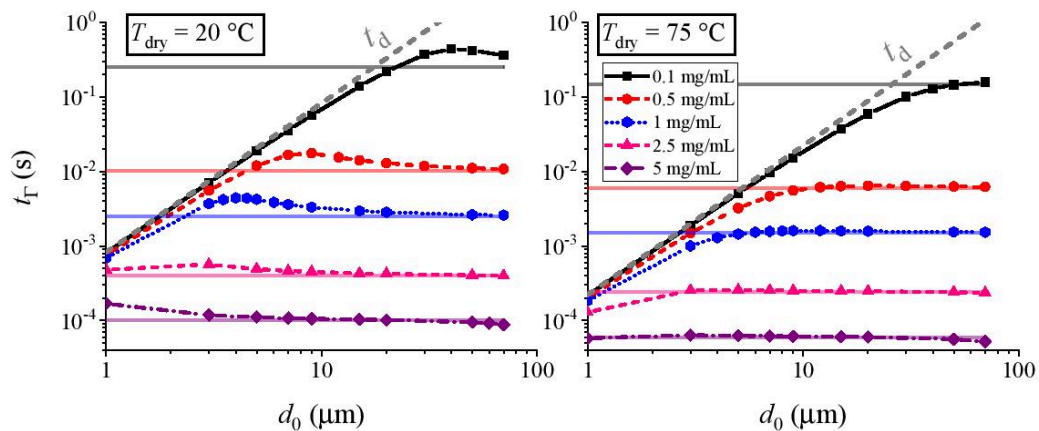


707

708

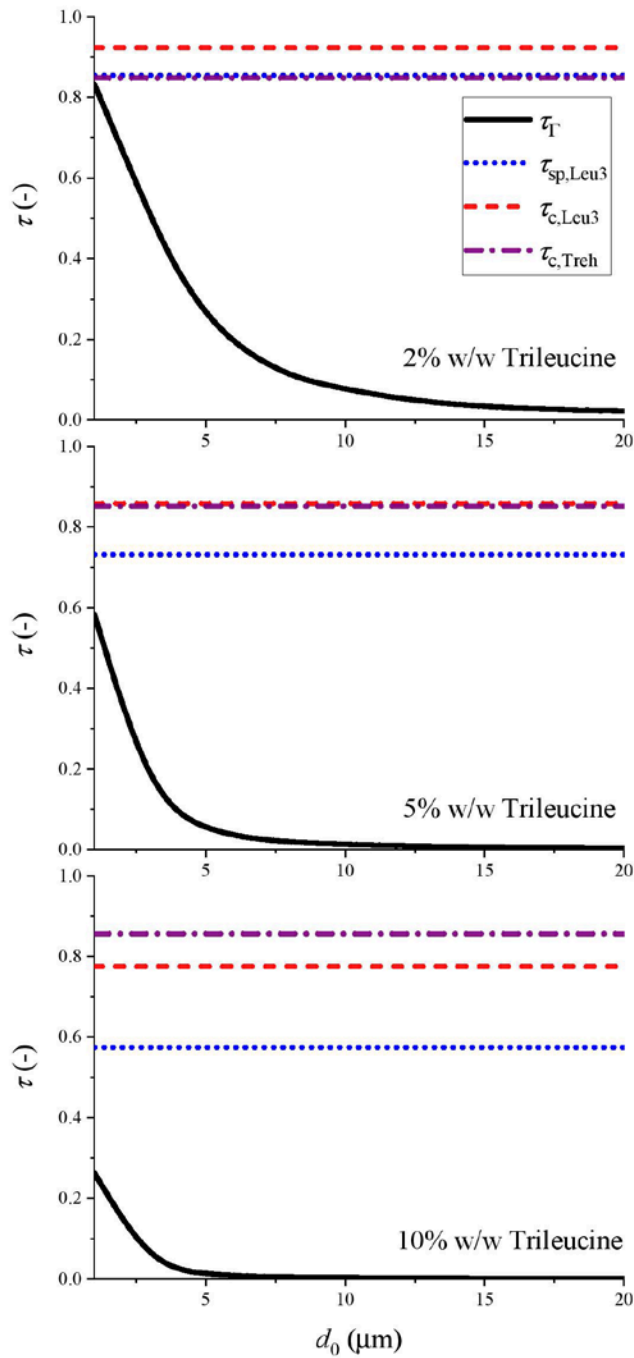
(b)

709 *Figure 12* (a) The bulk and subsurface concentrations as well as the instantaneous surface excess of a water droplet containing 1  
 710 mg/mL trileucine, drying at 75 °C with an initial diameter of 8 μm. For this specific droplet, the drying time was calculated to be  
 711 0.014 s. (b) The internal concentration distribution at different times for the same droplet of (a) versus the normalized radial  
 712 coordinate.



713

714 *Figure 13* The calculated time required for trileucine monolayer formation for different trileucine feed concentrations and initial  
 715 droplet diameters at two different drying temperatures. The curves were obtained from the solution of the diffusion equations  
 716 inside an evaporating droplet. The horizontal asymptotic lines were obtained from equation 4 and  $t_d = d_0^2/\kappa$  is the droplet  
 717 lifetime.



718

719 *Figure 14* The different dimensionless timescales of three trileucine/trehalose systems with a total feed concentration of 50  
 720 mg/mL and varying fractions of trileucine.  $\tau_T = t_r/t_d$  is the time required for the formation of a saturated trileucine monolayer  
 721 on the surface of the droplets.  $\tau_{sp,Leu3}$  is the approximate time when spinodal decomposition of trileucine is predicted to start.  
 722  $\tau_{c,Leu3}$  is the predicted time for trileucine to make a rigid shell on the surface and  $\tau_{c,Treh}$  is the approximate time at which  
 723 trehalose is expected to solidify. The drying temperature was 75 °C for all cases.

724

725

## 726 **4. Conclusion**

727 A methodology was proposed to implement the effect of surface activity into available particle formation  
728 models for the first time. Furthermore, the particle formation of trileucine, a surface-active molecule that  
729 does not crystallize during spray drying and has low aqueous solubility, was explained as a combination  
730 of the formation of an adsorbed monolayer on the droplet surface and liquid-liquid phase separation due  
731 to spinodal decomposition.

732 The formation of a fully saturated monolayer of trileucine on the droplet surface contributes to the  
733 significant improvement of aerosol properties. The highly wrinkled morphologies and low densities  
734 observed for systems containing trileucine as a dispersibility enhancer were also explained as having been  
735 caused by the early phase separation.

736 By following the methodology explained in this study and combining the information obtained from  
737 experimentation and theoretical discussions, a formulator can design a system with minimal experimental  
738 iterations with trileucine as a dispersibility enhancer in systems containing other excipients and active  
739 pharmaceutical ingredients.

740

## 741 **Acknowledgments**

742 FKAG and JPR acknowledge support from the Engineering and Physical Sciences Research Council  
743 under grant code EP/N025245/1.

## 744 **References**

- 745 [1] M. Davis, G. Walker, Recent strategies in spray drying for the enhanced bioavailability of poorly  
746 water-soluble drugs, *J. Control. Release.* 269 (2018) 110–127.  
747 <https://doi.org/10.1016/J.JCONREL.2017.11.005>.
- 748 [2] N. Carrigy, R. Vehring, Engineering Stable Spray-Dried Biologic Powder for Inhalation, in: A.J.  
749 Hickey, S.R. da Rocha (Eds.), *Pharm. Inhal. Aerosol Technol.*, third, CRC Press, Boca Raton,  
750 Florida, 2019: pp. 291–236.
- 751 [3] A. Dabbagh, N.H. Abu Kasim, C.H. Yeong, T.W. Wong, N. Abdul Rahman, Critical Parameters  
752 for Particle-Based Pulmonary Delivery of Chemotherapeutics, *J. Aerosol Med. Pulm. Drug Deliv.*  
753 31 (2018) 139–154. <https://doi.org/10.1089/jamp.2017.1382>.
- 754 [4] W.H. Finlay, *The Mechanics of Inhaled Pharmaceutical Aerosols: an Introduction*, 2nd ed.,  
755 Elsevier, 2019.
- 756 [5] N. Islam, M.J. Cleary, Developing an efficient and reliable dry powder inhaler for pulmonary drug  
757 delivery – A review for multidisciplinary researchers, *Med. Eng. Phys.* 34 (2012) 409–427.  
758 <https://doi.org/10.1016/j.medengphy.2011.12.025>.
- 759 [6] O.N. Ógáin, J. Li, L. Tajber, O.I. Corrigan, A.M. Healy, Particle engineering of materials for oral  
760 inhalation by dry powder inhalers. I—Particles of sugar excipients (trehalose and raffinose) for  
761 protein delivery, *Int. J. Pharm.* 405 (2011) 23–35.  
762 <https://doi.org/10.1016/J.IJPHARM.2010.11.039>.
- 763 [7] P.T. Mah, P. O’Connell, S. Focaroli, R. Lundy, T.F. O’Mahony, J.E. Hastedt, I. Gitlin, S.  
764 Oscarson, J. V. Fahy, A.M. Healy, The use of hydrophobic amino acids in protecting spray dried  
765 trehalose formulations against moisture-induced changes, *Eur. J. Pharm. Biopharm.* 144 (2019)  
766 139–153. <https://doi.org/10.1016/j.ejpb.2019.09.014>.

- 767 [8] N.B. Carrigy, M. Ordoubadi, Y. Liu, O. Melhem, D. Barona, H. Wang, L. Milburn, C.A. Ruzycki,  
768 W.H. Finlay, R. Vehring, Amorphous pullulan trehalose microparticle platform for respiratory  
769 delivery, *Int. J. Pharm.* 563 (2019) 156–168. <https://doi.org/10.1016/j.ijpharm.2019.04.004>.
- 770 [9] A.L. Feng, M.A. Boraey, M.A. Gwin, P.R. Finlay, P.J. Kuehl, R. Vehring, Mechanistic models  
771 facilitate efficient development of leucine containing microparticles for pulmonary drug delivery,  
772 *Int. J. Pharm.* 409 (2011) 156–163. <https://doi.org/10.1016/j.ijpharm.2011.02.049>.
- 773 [10] X.-F. Yang, Y. Xu, D.-S. Qu, H.-Y. Li, The influence of amino acids on aztreonam spray-dried  
774 powders for inhalation, *Asian J. Pharm. Sci.* 10 (2015) 541–548.  
775 <https://doi.org/10.1016/j.ajps.2015.08.002>.
- 776 [11] M. Ordoubadi, F.K.A. Gregson, H. Wang, M. Nicholas, S. Gracin, D. Lechuga-Ballesteros, J.P.  
777 Reid, W.H. Finlay, R. Vehring, On the particle formation of leucine in spray drying of inhalable  
778 microparticles, *Int. J. Pharm.* 592 (2021) 120102. <https://doi.org/10.1016/j.ijpharm.2020.120102>.
- 779 [12] D. Lechuga-Ballesteros, C. Charan, C.L.M. Stults, C.L. Stevenson, D.P. Miller, R. Vehring, V.  
780 Tep, M. Kuo, Trileucine Improves Aerosol Performance and Stability of Spray-Dried Powders for  
781 Inhalation, *J. Pharm. Sci.* 97 (2008) 287–302. <https://doi.org/10.1002/jps.21078>.
- 782 [13] H. Wang, D.S. Nobes, R. Vehring, Particle Surface Roughness Improves Colloidal Stability of  
783 Pressurized Pharmaceutical Suspensions, *Pharm. Res.* 36 (2019) 43.  
784 <https://doi.org/10.1007/s11095-019-2572-0>.
- 785 [14] I. Sibum, P. Hagedoorn, M.P.G. Kluitman, M. Kloezen, H.W. Frijlink, F. Grasmeijer,  
786 Dispersibility and Storage Stability Optimization of High Dose Isoniazid Dry Powder Inhalation  
787 Formulations with L-Leucine or Trileucine, *Pharmaceutics.* 12 (2019) 24.  
788 <https://doi.org/10.3390/pharmaceutics12010024>.
- 789 [15] R. Vehring, Pharmaceutical Particle Engineering via Spray Drying, *Pharm. Res.* 25 (2008) 999–

- 790 1022. <https://doi.org/10.1007/s11095-007-9475-1>.
- 791 [16] M. Gomez, J. McCollum, H. Wang, M. Ordoubadi, C. Jar, N.B. Carrigy, D. Barona, I. Tetreau, M.  
792 Archer, A. Gerhardt, C. Press, C.B. Fox, R.M. Kramer, R. Vehring, Development of a formulation  
793 platform for a spray-dried, inhalable tuberculosis vaccine candidate, *Int. J. Pharm.* 593 (2021)  
794 120121. <https://doi.org/10.1016/j.ijpharm.2020.120121>.
- 795 [17] N.B. Carrigy, L. Liang, H. Wang, S. Kariuki, T.E. Nagel, I.F. Connerton, R. Vehring, Trileucine  
796 and Pullulan Improve Anti-Campylobacter Bacteriophage Stability in Engineered Spray-Dried  
797 Microparticles, *Ann. Biomed. Eng.* (2019). <https://doi.org/10.1007/s10439-019-02435-6>.
- 798 [18] M.A. Boraey, R. Vehring, Diffusion controlled formation of microparticles, *J. Aerosol Sci.* 67  
799 (2014) 131–143. <https://doi.org/10.1016/j.jaerosci.2013.10.002>.
- 800 [19] R. Vehring, W.R. Foss, D. Lechuga-Ballesteros, Particle formation in spray drying, *J. Aerosol Sci.*  
801 38 (2007) 728–746. <https://doi.org/10.1016/j.jaerosci.2007.04.005>.
- 802 [20] M.A. Boraey, S. Hoe, H. Sharif, D.P. Miller, D. Lechuga-Ballesteros, R. Vehring, Improvement of  
803 the dispersibility of spray-dried budesonide powders using leucine in an ethanol–water cosolvent  
804 system, *Powder Technol.* 236 (2013) 171–178. <https://doi.org/10.1016/j.powtec.2012.02.047>.
- 805 [21] P. Seydel, J. Blömer, J. Bertling, Modeling particle formation at spray drying using population  
806 balances, *Dry. Technol.* 24 (2006) 137–146. <https://doi.org/10.1080/07373930600558912>.
- 807 [22] P.G. Vekilov, Nucleation, *Cryst. Growth Des.* 10 (2010) 5007–5019.  
808 <https://doi.org/10.1021/cg1011633>.
- 809 [23] F.K.A. Gregson, M. Ordoubadi, R.E.H. Miles, A.E. Haddrell, D. Barona, D. Lewis, T. Church, R.  
810 Vehring, J.P. Reid, Studies of competing evaporation rates of multiple volatile components from a  
811 single binary-component aerosol droplet, *Phys. Chem. Chem. Phys.* (2019).  
812 <https://doi.org/10.1039/C9CP01158G>.

- 813 [24] M. Ordoubadi, F.K.A. Gregson, O. Melhem, D. Barona, R.E.H. Miles, D. D'Sa, S. Gracin, D.  
814 Lechuga-Ballesteros, J.P. Reid, W.H. Finlay, R. Vehring, Multi-Solvent Microdroplet  
815 Evaporation: Modeling and Measurement of Spray-Drying Kinetics with Inhalable Pharmaceuticals,  
816 *Pharm. Res.* 36 (2019) 100. <https://doi.org/10.1007/s11095-019-2630-7>.
- 817 [25] A. Baldelli, R. Vehring, Control of the radial distribution of chemical components in spray-dried  
818 crystalline microparticles, *Aerosol Sci. Technol.* 50 (2016) 1130–1142.  
819 <https://doi.org/10.1080/02786826.2016.1216941>.
- 820 [26] A. Baldelli, M.A. Boraey, D.S. Nobes, R. Vehring, Analysis of the Particle Formation Process of  
821 Structured Microparticles, *Mol. Pharm.* 12 (2015) 2562–2573. <https://doi.org/10.1021/mp500758s>.
- 822 [27] A. Haddrell, G. Rovelli, D. Lewis, T. Church, J. Reid, Identifying time-dependent changes in the  
823 morphology of an individual aerosol particle from its light scattering pattern, *Aerosol Sci.*  
824 *Technol.* (2019) 1–18. <https://doi.org/10.1080/02786826.2019.1661351>.
- 825 [28] M. Ordoubadi, F. Gregson, W.H. Finlay, R. Vehring, J.P. Reid, Interaction of evaporating  
826 multicomponent microdroplets with humid environments, in: *Respir. Drug Deliv.*, 2018.
- 827 [29] MATLAB, version 9.6.0 (R2019a), The MathWorks Inc., Natick, Massachusetts, 2019.
- 828 [30] S. Hoe, J.W. Ivey, M.A. Boraey, A. Shamsaddini-Shahrbabak, E. Javaheri, S. Matinkhoo, W.H.  
829 Finlay, R. Vehring, Use of a Fundamental Approach to Spray-Drying Formulation Design to  
830 Facilitate the Development of Multi-Component Dry Powder Aerosols for Respiratory Drug  
831 Delivery, *Pharm. Res.* 31 (2014) 449–465. <https://doi.org/10.1007/s11095-013-1174-5>.
- 832 [31] C.A. Schneider, W.S. Rasband, K.W. Eliceiri, NIH Image to ImageJ: 25 years of image analysis,  
833 *Nat. Methods.* 9 (2012) 671–675. <https://doi.org/10.1038/nmeth.2089>.
- 834 [32] H. Wang, D. Barona, S. Oladepo, L. Williams, S. Hoe, D. Lechuga-Ballesteros, R. Vehring,  
835 Macro-Raman spectroscopy for bulk composition and homogeneity analysis of multi-component

- 836 pharmaceutical powders, *J. Pharm. Biomed. Anal.* 141 (2017) 180–191.  
837 <https://doi.org/10.1016/j.jpba.2017.04.003>.
- 838 [33] S. Muramoto, J. Brison, D.G. Castner, Exploring the Surface Sensitivity of TOF-Secondary Ion  
839 Mass Spectrometry by Measuring the Implantation and Sampling Depths of Bi n and C 60 Ions in  
840 Organic Films, *Anal. Chem.* 84 (2012) 365–372. <https://doi.org/10.1021/ac202713k>.
- 841 [34] M. Nicholas, M. Josefson, M. Fransson, J. Wilbs, C. Roos, C. Boissier, K. Thalberg,  
842 Quantification of surface composition and surface structure of inhalation powders using TOF-  
843 SIMS, *Int. J. Pharm.* 587 (2020) 119666. <https://doi.org/10.1016/j.ijpharm.2020.119666>.
- 844 [35] R. Miller, V.B. Fainerman, V. Pradines, V.I. Kovalchuk, N.M. Kovalchuk, E. V Aksenenko, L.  
845 Liggieri, F. Ravera, G. Loglio, A. Sharipova, Y. Vysotsky, D. Vollhardt, N. Mucic, R. Wüstneck,  
846 J. Krägel, A. Javadi, 4 Surfactant Adsorption Layers at Liquid Interfaces, in: *Surfactant Sci.*  
847 *Technol.*, CRC Press, 2014: pp. 149–169.
- 848 [36] J. Eastoe, J.. Dalton, Dynamic surface tension and adsorption mechanisms of surfactants at the air–  
849 water interface, *Adv. Colloid Interface Sci.* 85 (2000) 103–144. [https://doi.org/10.1016/S0001-](https://doi.org/10.1016/S0001-8686(99)00017-2)  
850 [8686\(99\)00017-2](https://doi.org/10.1016/S0001-8686(99)00017-2).
- 851 [37] K. Landström, J. Alsins, B. Bergenståhl, Competitive protein adsorption between bovine serum  
852 albumin and  $\beta$ -lactoglobulin during spray-drying, *Food Hydrocoll.* 14 (2000) 75–82.  
853 [https://doi.org/10.1016/S0268-005X\(99\)00047-8](https://doi.org/10.1016/S0268-005X(99)00047-8).
- 854 [38] M. Jayasundera, B. Adhikari, P. Aldred, A. Ghandi, Surface modification of spray dried food and  
855 emulsion powders with surface-active proteins: A review, *J. Food Eng.* 93 (2009) 266–277.  
856 <https://doi.org/10.1016/j.jfoodeng.2009.01.036>.
- 857 [39] Y. He, P. Yazhgur, A. Salonen, D. Langevin, Adsorption–desorption kinetics of surfactants at  
858 liquid surfaces, *Adv. Colloid Interface Sci.* 222 (2015) 377–384.

- 859 <https://doi.org/10.1016/j.cis.2014.09.002>.
- 860 [40] A.F.H. Ward, L. Tordai, Time-Dependence of Boundary Tensions of Solutions I. The Role of  
861 Diffusion in Time-Effects, *J. Chem. Phys.* 14 (1946) 453–461. <https://doi.org/10.1063/1.1724167>.
- 862 [41] B.R. Bzdek, J.P. Reid, J. Malila, N.L. Prisle, The surface tension of surfactant-containing, finite  
863 volume droplets, *Proc. Natl. Acad. Sci.* 117 (2020) 8335–8343.  
864 <https://doi.org/10.1073/pnas.1915660117>.
- 865 [42] M. Nuzzo, A. Millqvist-Fureby, J. Sloth, B. Bergenstahl, Surface Composition and Morphology of  
866 Particles Dried Individually and by Spray Drying, *Dry. Technol.* 33 (2015) 757–767.  
867 <https://doi.org/10.1080/07373937.2014.990566>.
- 868 [43] J. Malila, N.L. Prisle, A monolayer partitioning scheme for droplets of surfactant solutions, *J.*  
869 *Adv. Model. Earth Syst.* 10 (2018) 2018MS001456. <https://doi.org/10.1029/2018MS001456>.
- 870 [44] M. Meere, G. Pontrelli, S. McGinty, Modelling phase separation in amorphous solid dispersions,  
871 *Acta Biomater.* 94 (2019) 410–424. <https://doi.org/10.1016/j.actbio.2019.06.009>.
- 872 [45] D. Gebauer, M. Kellermeier, J.D. Gale, L. Bergström, H. Cölfen, Pre-nucleation clusters as solute  
873 precursors in crystallisation, *Chem. Soc. Rev.* 43 (2014) 2348–2371.  
874 <https://doi.org/10.1039/C3CS60451A>.
- 875 [46] P.C. Hiemenz, T.P. Lodge, Thermodynamics of Polymer Solutions, in: *Polym. Chem.*, 2nd ed.,  
876 CRC Press, Boca Raton, 2007: pp. 247–288.  
877 <http://ebookcentral.proquest.com/lib/ualberta/detail.action?docID=1447077>.
- 878 [47] T. Lindvig, M.L. Michelsen, G.M. Kontogeorgis, A Flory–Huggins model based on the Hansen  
879 solubility parameters, *Fluid Phase Equilib.* 203 (2002) 247–260. [https://doi.org/10.1016/S0378-](https://doi.org/10.1016/S0378-3812(02)00184-X)  
880 [3812\(02\)00184-X](https://doi.org/10.1016/S0378-3812(02)00184-X).
- 881 [48] C.M. Hansen, *Hansen Solubility Parameters: A User’s Handbook*, Second Edition, CRC Press,

- 882 2007. <https://doi.org/10.1201/9781420006834>.
- 883 [49] D.W. Van Krevelen, K. Te Nijenhuis, Chapter 7 - Cohesive Properties and Solubility, in: Prop.  
884 Polym. - Their Correl. with Chem. Struct. Their Numer. Estim. Predict. from Addit. Gr. Contrib.,  
885 4th ed., Elsevier, Amsterdam, 2009: pp. 189–227. [https://doi.org/10.1016/B978-0-08-054819-](https://doi.org/10.1016/B978-0-08-054819-7.00007-8)  
886 [7.00007-8](https://doi.org/10.1016/B978-0-08-054819-7.00007-8).
- 887 [50] M.A. Freedman, Phase separation in organic aerosol, Chem. Soc. Rev. 46 (2017) 7694–7705.  
888 <https://doi.org/10.1039/C6CS00783J>.
- 889